Targeting IL-6/IL-6R Signaling Axis in Triple-Negative Breast Cancer by a Novel Nifetepimine-Loaded Cascade Ph Responsive Mesoporous Silica Based Nanoplatform

Suman Bhandary[1], Arijit Bhowmik[2], Aparajita Ghosh[1], Suchandrima Saha[3], Uttam Pal[4], Nivedita Roy[1], Nilanjan Chakraborty[5], Arijit Chakraborty[5], Mrinal K Ghosh[2] and Parimal C Sen[1]*

[1]Division of Molecular Medicine, India

[2]Cancer Biology and Inflammatory Disorder, India

[3]Division of Drug Development Diagnostics and Biotechnology, India

[4]Chemical Sciences Division, Saha Institute of Nuclear Physics, India

[5]Department of Chemistry, Maulana Azad College, India

Submission: September 13, 2017; **Published:** October 27, 2017

***Corresponding author:** Parimal C Sen, Division of Molecular Medicine, India, Tel: +9133 25693222, Fax: +91332355-3886, Email: parimalsen.boseinst@gmail.com; parimal@jcbose.ac.in

Abstract

Triple negative breast cancer (TNBC) still remains the most aggressive and life-threatening cancer with poor prognosis among women. Herein, we fabricated a cascade pH-responsive, foliate functionalized mesoporous silica nanocarrier (MSN) with suitable PEG dynamic protection strategy for the targeted delivery of a hydrophobic anticancer agent, nifetepimine (NFT). *In vitro* studies showed that dissociation of gate keeper's boosted NFT release from functionalized MSN (fMSN), leading to mitochondria mediated apoptosis of TNBC cells. *In vivo* experimentation demonstrated that NFT-fMSNs exhibited tumor regression potential with negligible side effects deregulated the prime phenotypes associated with invasion and simultaneously reduced lung metastasis in breast tumor bearing BALB/c mice.

Recent findings report that IL-6 is one of the important pathways, that is involved in initiation and progression of highly aggressive TNBCs. Therefore, it is an intriguing pathway to study the potential impact of NFT-fMSNs on TNBC *in vitro* and in vivo. Here, we hypothesized that upon release from functionalized MSN, NFT molecules work by inhibiting IL-6 binding to their specific receptors on the cell surface thereby halting TNBC cell invasion and metastasis. Our study thus demonstrates an extensive justification for the effectiveness and the prospect of using NFT-f MSNs as an anticancer drug that can selectively target breast tumor cells and offer one of a kind solution to counter the challenges to the clinical translation of cancer nano medicines.

Keywords: Mesoporous silica nanoparticles; Nifetepimine; pH-responsive drug release;Interleukin-6 receptor; Apoptosis; Metastasis

Abbreviations: MSNs: Mesoporous Silica Nanoparticles; fMSNs: Functionalized Mesoporous Silica Nanoparticles; NFT: Nifetepimine; TNBC: Triple negative Breast Cancer; DDS: Drug Delivery System; PEG: Polyethylene Glycol; EPR: Enhanced Permeation and Retention; FA: Folic acid; FR: Folate Receptor; NFT- fMSNs: NFT Loaded Functionalized MSNs; β-CD: β-cyclodextrin; Ada:1-(Amino methyl)adamantine; mPEG: Polyethylene Glycol Monomethyl ether; ROS: Reactive Oxygen Species; H2DCF-DA,2′,7′: Dichloro Dihydrofluoresce in Diacetate; IL-6: Interleukin-6; MMPs: Matrix Metalloproteinase; VEGF: Vascular Endothelial Growth Factor; FESEM: Field Emission Scanning Electron Microscopy; TEM: Transmission Electron Microscopy; XPS: X-ray Photoelectron Spectroscopy; APTES: 3Aminopropyltriethoxysilane; XRD:X-ray Diffraction; FITC: Fluoresce in Iso Thio Cyanate; FITC- fMSNs: FITC-Labeled Functionalized Mesoporous Silica Nanoparticles; BET: Brunauer-Emmett-Teller; BJH: Barrett-Joyner-Halenda; SBET:BET Specific Surface Area; Vt: Total Pore Volume; WBJH: BJH Pore Diameter; DTA, Differential Thermal Analysis; TGA, Thermo Gravimetric Analysis; DMSO, Dimethyl sulfoxide; SXRD, Small-angle X-ray Diffraction; CLSM, Confocal Laser Scanning Microscopic; EDX: Energy-Dispersive X-ray Spectroscopy; ΔΨ m: Mitochondrial Trans Membrane potential; MPTPs: Mitochondrial Permeability Transition Pores; FACS: Fluorescence Activated Cell Sorting; MTT: (3-(4,5-Dimethylthiazol-2-yl)-2,5- Diphenyltetrazolium Bromide); TUNEL: Zerminal Deoxynucleotidyl Transverses dUTP Nick End Labeling; PBS: Phosphate Buffered Saline; PARP: Poly (ADP-ribose) Polymerase; ICP-OES: Inductively Coupled Plasma-Optical Emission Spectrometry; AST: Aspartate Amino Transferase; ALP: Alkaline Phosphates; ALT: Alkaline Amino Transferases; BUN: Blood Urea Nitrogen; CREAT: Creatinine.

Introduction

The survival outcomes of triple negative metastatic breast cancer (MBC) still pose a big menace to the conventional chemotherapeutic agents due to their inadmissible side effects and nonspecific biodistribution [1,2]. In our previous studies, we have identified nifetepimine (NFT) as a potential anticancer agent against TNBC cell Lines [3]. However, hydrophobicity, poor bioavailability and rapid systemic elimination of NFT have limited its clinical manifestations. Therefore, it is essential to develop an improved nanoparticle-based targeted drug delivery system (DDS) that can facilitate on-site release of NFT. Encapsulation of NFT in polymeric nanocapsules was found to have greater potential against TNBC [4].

However, the study had certain limitations due to the fact that surface modification of PLGA nanoparticles would be needed to promote their cellular uptake upon arrival at the target tissues and thus avoiding nonspecific distribution of NFT. Surface modification enhances tumor/organ target ability of nanoparticles thereby increasing selective cellular binding and internalization through receptor-mediated endocytosis. Mesoporous silica nanoparticles (MSNs) offer a great platform in targeted delivery of therapeutics by focusing on cascade pH-responsive controlled release of drugs via removable gatekeepers to cap the pores. Their unique features highlight excellent biocompatibility, high loading capacity of poorly water soluble cargo and attachment of organic surface functionalities [5,6].

The caps can be removed via redox reactions, pH changes or light-sensitive release [7-9]. Surface fictionalization of these MSN nanocarriers with methoxy polyethylene glycol (mPEG) shielding makes it more competent for penetrating cancer cells across leaky vasculatures of tumor tissues through enhanced permeation and retention (EPR) effect [10,11]. Studies have shown that most primary and metastatic cancer (80% of metastatic TNBCs) tissues display over expressed folate receptor (FR) [12,13]. Folic acid (FA) is a great putative marker for cancer diagnosis and therapy, and has high binding affinity towards FR, lack of immunogenicity, high stability and low cost [14-16]. Therefore, surface fictionalization of DDSs with folic acid happens to be a promising strategy for cancer therapy.

Moreover, the acidic extracellular/interstitial pH which is an indication of tumor malignancy, has emerged as a stimulus for the design of pH-responsive DDSs resulting in site-selective controlled release of the loaded cargo from the MSN system. The acidic pH found in the tumor microenvironment (pH ~6.8) is mainly the aftereffect of irregular angiogenesis in fast-growing tumors. Acidic environment of the tumor interstitial tissue (pH 5-6) provides a potential internal trigger for the release of cargo molecules from DDSs [17]. The pH-sensitive gatekeepers remain closed at pH 7.4 but open at low pH, promoting endosomal escape and ensuring cytosolic release of the encapsulated drug [18,19]. This pH responsiveness is an excellent factor for parenteral administration of drugs [17,18].

Recent studies suggest that over-expression of interleukin-6 (IL-6) may contribute to angiogenesis by up-regulating pro-angiogenic molecules, including vascular endothelial growth factor (VEGF) and its receptor [20]. High levels of IL-6 are associated with development of metastasis and multidrug resistance in TNBC with poor prognosis [21-24]. This increased level of IL-6, accompanied by increased expression of matrix metalloproteinase's (MMPs), including the gelatinizes MMP-2 and MMP-9, support not only vascular remodeling in primary tumors, but also lung extravasations, tumor cell invasion and metastasis due to their ability to degrade the extracellular matrix [25-28].

Therefore, targeting of IL-6 and its receptor in cancer has a strong biological rationale, and may serve as a novel target in the therapeutic intervention of MBC. In the present study, we attempt to prepare a pH cascade responsive, folates functionalized MSN nano formulations of NFT (NFT-fMSNs) and establish its mechanistic role in restraining tumor cell invasion and metastasis via IL-6R targeting in TNBC.

Materials and Methods

Experimental materials

All reagents were purchased from commercial suppliers: Guaranteed grade 3-aminopropyltriethoxysilane (APTES), tetraethyl orthosilicate (TEOS), fluoresce in isothiocyanate (FITC), Cetyl trimethyl ammonium bromide (CTAB), anhydrous N,N-dimethyl formamide (DMF), N-hydroxyl succinimide (NHS), N-(3-dimethylaminopropyl)-N- ethyl carbodiimide hydrochloride (EDC), folic acid (FA), 4-formylbenzoic acid, 4-carboxyphenylboronic acid (CBA), Polyethylene glycol monomethyl ether (mPEG, average MW 2000), 3-(3,4-dihydroxyphenyl) prop ionic acid (DHPA), 1-(Amino methyl) adamantine (Ada), N,N-diethyl ethanamine (DEE), dichloromethane (DCM), 6-diamidino-2-phenylindole dihydrochloride (DAPI), dichlorodihydrofluoresce in diacetate (DCF-DA), Histopaque-1077, Calcein-AM, Mitomycin C, Cytochalas in B were purchased from Sigma-Aldrich (St. Louis, MO, USA) and used as received.

Nonessential amino acids, L-glutamine, penicillin, streptomycin, gentamycin, trypsin-EDTA, 3-(4,5-Dimethyl-thiazol-2-yl)-2,5-diphenyl-tetrazolium bromide (MTT), bovine serum albumin and Dulbecco's modified Eagle's medium (DMEM), RPMI1640, Phosphate Buffered Saline, pH 7.4 1X, Product Code: TL1101 were purchased from HIMEDIA(Mumbai, India). Antibodies were obtained from Santa Cruz Biotechnology and Cell Signaling Technology (USA). HPLC-grade methanol, acetonitrile and phosphoric acid were purchased from Merck (Germany).

RPMI 1640 without folic acid, RPMI 1640 without phenol red, fetal bovine serum (FBS) was purchased from *In vitro*

gen (Carlsbad, CA, USA). Mito Tracker Red, Lisa tracker Red, Rhodamine-Phalloid in and Fluo-3 AM were purchased from Molecular Probes by Life Technologies (Carlsbad, CA). All other chemicals and solvents were commercially available and used as purchased without further purification. Nanopure water (Millipore Co., USA) was used in all experiments and to prepare all buffers and mediums. Vecta shield ant fade mounting medium with and without DAPI was purchased from Vector Laboratories Ltd, United Kingdom.

Cell lines and culture conditions

Breast cancer cell lines (MDA-MB-231, MDA-MB-468 and 4T1) were obtained from NCCS (Pune, India) and used at passages 24-30. MCF 10A cell line was a kind gift from Prof. Tamara Lah and Dr. Neža Podergajs, National Institute of Biology, Ljubljana, Slovenia. The cell lines (except MCF 10A) were maintained in DMEM or RPMI 1640 supplemented with 10% FBS and 1% penicillin/streptomycin/gentamycin at 37 °C in CO_2 incubator in an atmosphere of humidified 5% CO_2 and 95% air. The cells were maintained by routine sub culturing in tissue culture flasks. The culture medium was changed every 48h and the cells were split when they reached confluence. Cells from exponentially growing cultures were used for all the experiments.

Experimental Procedures

Synthesis of nifetepimine (NFT)

Nifetepimine was synthesized in our laboratory via the original protocol for synthesis of dihydro pyrimidinones [29] and as reported earlier from our laboratory [30] and confirmed to be >98% pure after NMR and FTIR spectroscopy (Figure S1a & b).
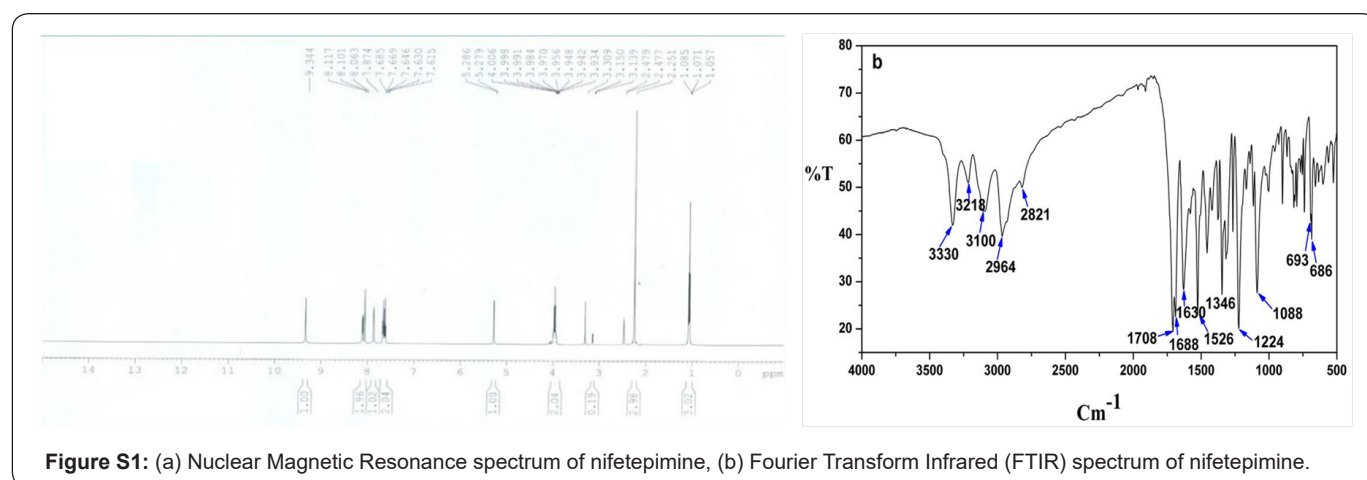

Figure S1: (a) Nuclear Magnetic Resonance spectrum of nifetepimine, (b) Fourier Transform Infrared (FTIR) spectrum of nifetepimine.

Synthesis of aminopropyl functionalized fluorescent mesoporous silica nanoparticles

MSNs were prepared by a previously described CATB-templated, base-catalyzed sol-gel method with slight modifications [31,32]. Briefly, 200mg of CTAB was dissolved in a mixture of milli Q water (96mL) and 25%ammonium hydroxide. The pH value was adjusted to ~11 and reaction temperature was raised to 80 °C, stirred vigorously and kept at that temperature for 30min. Once the temperature of the CTAB solution was stabilized, TEOS (1mL) were added to the mixture drop wise and then 3-aminopropyltriethoxysilane, APTES (140μL) was subsequently added to the solution rapidly. The solution turned from clear to opaque, indicative of a hydrolysis process.

After 2h, the sample was centrifuged and washed thoroughly with milli Q water and ethanol three times each. The particles were allowed to dry at room temperature overnight. Surfactant removal was performed by refluxing in acidic methanol (9mL of HCl/400mL of methanol) for 24h at 70 °C, which were further centrifuged, washed several times with ethanol and water and then dried under vacuum for 24h. The product was denoted as AP-MSNs. The synthesis of MSNs is as the same as that of AP-MSNs except addition of APTES. Fluorescent dye molecules were introduced into silica nanoparticles by using a thiourea-linkage forming reaction through APTES and dye molecules having an isothiocyanate functional group, i.e. rhodamine isothiocyanate (RITC) and fluoresce in isothiocyanate (FITC) to visualize the cellular uptake [33].

Synthesis of boronic acid functionalized AP-MSNs

AP-MSNs were functionalized with CBA following the protocol of Luo et al. [34,35]. For the synthesis, 80 mg of CBA was first dissolved in 10mL DMSO followed by the addition of EDC (100mg) and NHS (50mg), and stirred for 30min. Afterwards, AP-MSNs solution (0.2g in 10mL DMSO) was added drop wise to the activated CBA solution under vigorous stirring at room temperature for approximately 24h. The synthesized solid product was then collected by centrifugation and extensively washed five times with milli Q water. The product was denoted as BA-MSNs.

Synthesis of β-CD-catechol

Mono-amino- modified cyclo dextrin (β-CD-NH$_2$) was prepared as described in the literature [36,37]. Catechol modification of β-cyclodextrin (β-CD-catechol) was performed according to a previously published protocol with minor modification [38]. Briefly, 0.8mM DHPA was dissolved into hexamethylenetetramine/HCl buffer solution (pH 5.5) containing

EDC and NHS. The solution was stirred at room temperature under inert atmosphere for 1h, 0.5g of β-CD-NH$_2$ was added into the above solution and stirred for another 24h under inert atmosphere. The mixture was added drop wise to acetone and precipitated into cold diethyl ether. Then subsequent dialysis and lyophilization were performed to obtain pure final product.

Synthesis of methoxy poly(ethylene glycol) benzaldehyde (mPEG-CHO)

MPEG-CHO was synthesized according to a reference procedure [39]. Typically 5.0g of mPEG was dissolved in150mL of dichloromethane followed by addition of 3.0 g of 4-formylbenzoic acid, 4.2g of DCC and 0.32g of DMAP. The mixture was stirred for another 24h at room temperature. After that, the suspension was removed and the solvent of the filtrate was removed by rotary evaporation. The white powder obtained was again suspended in 25mL of milli Q water. The aqueous solution was extracted with dichloromethane and the combined organic layers were dried over sodium sulphate, concentrated and precipitated through 100mL of cold diethyl ether to yield a white solid, mPEG-CHO.

Synthesis of mPEG-Ada

MPEG-Ada was synthesized based on the published protocol by Wang et al. [40]. 1-adamantanemethylamine (Ada) (100mg) was dissolved in DMSO (5mL). MPEG-CHO (1g) was dissolved into 10mL of DMSO. The above two solutions were slowly mixed and the reaction was stirred for 3h at 50 °C. Subsequently, the solvent was removed by rotary evaporation and rinsed with diethyl ether and methanol 3 times each. Finally it was lyophilized to obtain mPEG-Ada as a white powder.

Synthesis of N-adamantyl folate amide (FA-Ada)

FA-Ada was synthesized following the protocol of Yen Ang et al. [41]. Firstly, activation of folic acid (250mg) in DMF was performed by EDC (73mg) and NHS (65mg), and the reaction was allowed to proceed at room temperature for 24h. Separately, a mixture of Ada (10^{5}mg) and DEE (75mL) in DMF was stirred for 4h prior to the addition to the above solution, and the resulting mixture was stirred for two more days. Thereafter, the reaction mixture was precipitated in 30% acetone in diethyl ether and purified via column chromatography with silica gel to obtain FA-Ada.

Synthesis of NFT- loaded β-CD and FA functionalized PEG shielded pH responsive MSNs (NFT-fMSNs)

To load NFT, 50mg BA-MSNs was dispersed in 25mL DMSO solution of NFT (25mg). The mixture was stirred at room temperature for 24h. The product was centrifuged, washed with methanol and milli Q water, and lyophilized to give NFT- loaded BA-MSNs. Then 50mg of β-CD-catechol was dissolved in 25mL aqueous suspension of NFT-BA-MSNs (50 mg), and the reaction was continued at room temperature for another 24h. The resulting solid was centrifuged, washed with milli Q water, dried under vacuum to get NFT- loaded BA-MSNs-β-CD. NFT- loaded BA-MSNs-β-CD (25mg) was dispersed into 15mL 1X PBS (pH 7.4), followed by addition of FA-Ada and mPEG-Ada. The mixture was stirred at room temperature for a day. The suspension was denoted as NFT-fMSNs.

In vitro Study

Determination of percentage of drug loading into surface functionalized MSNs

Freeze-dried nanoparticles were dissolved in phosphate buffer solution (PBS, pH 7.4) and the percentage of Drug (NFT) loading (DL %) was determined by UV-Vis spectroscopy at 275nm (Shimadzu UV 1800) following equation 1:

$$DL\% = \frac{\left([NFT] - [NFT]_f\right)}{[NFT]_t} \times 100$$

Where the total concentration of NFT (free + encapsulated) in the system, [NFT]t, and that in the filtrate, [NFT]f.

In vitro pH-driven controlled release of NFT from fMSNs

The *in vitro* release experiments were performed in PBS at different pH (pH 7.4, 6.8 and 5.0). For each study, 5mg of NFT-fMSNs was suspended in 5mL of PBS, and the suspension was transferred to dialysis bag which was directly immersed into 20mL of PBS with the indicated pH value and gently stirred at 37 °C. At predetermined time point, 1mL aliquot was taken out from the solution and the volume of solution was kept constant by adding 1mL of PBS after each sampling. The amount of released NFT at each time point was determined using a UV-Vis spectrophotometer (Shimadzu UV 1800, Japan). The percent release of NFT at each time point was calculated by using equation 2

$$\% \mathrm{Re}lease = \frac{[NFT]_t}{[NFT]_\theta} \times 100$$

Where $[NFT]$ is the concentration of nifetepimine at time t.

In vitro stability study of the nanoformulations in buffer solutions of different pH value

The stability of nanoformulations is crucial for *in vitro* long-term storage and transportation, *in vivo* targeting, and long term blood circulation. 5mg of fMSNs was dispersed in 5mL of PBS (pH 5.0, 7.4 and 9.0), subsequently sonicated for 10min. The nanoformulations were placed at 37 °C, and size distribution and zeta potential changes were detected by DLS.

In vitro stability study of the nanoformulations in human plasma

For the stability studies in human blood, 1 mg of fMSNs was dispersed in 4500μL of PBS (pH 7.4) and 500μL of human

plasma, and left under stirring at 1000 rpm at 37 °C for 2h. Sample aliquots of 200μL were withdrawn at pre-determined time points (1, 5, 10, 20, 30, 60, 90, and 120min), and the corresponding Z-average value, PDI and zeta-potential were subsequently determined by Dynamic Light Scattering (DLS).

Plasma coagulation study

Prothombin time (PT) test was performed to study the possibility of any significant interference with normal blood coagulation time by the synthesized fMSNs following the published protocol [42].

Hemolysis study

The effect of mesoporous silica materials on hemolytic activity is important in order to understand how the materials will interact with blood. Hemolysis experiments were performed according to the published protocol [43]. EDTA stabilized human blood samples were collected from healthy volunteers of Bose Institute, Kolkata, India. First, 3mL of blood was centrifuged at 1600rpm for 5min and blood plasma and the surface layer were removed. The remaining RBC pellet was washed thrice with 3mL of PBS solution and RBCs were diluted in 15mL of PBS solution. Then, 0.8mL of MSN solutions in PBS at different concentrations were added to 0.2mL of RBC suspension.

Also, positive and negative controls were prepared by adding 0.8mL of 0.2% Triton X-100 and 0.9% normal saline, respectively to 0.2mL of RBC solution. Then, the samples were incubated at room temperature for 2h; they were slightly shaken once for every 30min to re-suspend the RBCs and MSNs. After 2h, they were centrifuged at 1600rpm and 100μL of supernatants was transferred to a 96-well plate. Absorbance of hemoglobin in supernatants was measured with a micro plate reader at 570 nm. Hemolysis percentages of the RBCs were calculated using the following formula 3**'**

$$\%Hemolysis = \frac{(absorbance\ of\ sample\ -\ absorbance\ of\ negative\ control)}{absorbance\ of\ positive\ control\ -\ absorbance\ of\ negative\ control}$$

mPEG leaving study

The mPEG leaving study was performed in 1X PBS with different pH values (pH 7.4 and 6.0), respectively. For each study, 5mg of fMSNs was suspended in 5mL of PBS, and was shaken in a water bath at 37 °C. The nano formulation was centrifuged and withdrawn from the solution periodically and was then washed with milli Q water twice. The resultant nanoparticles were then suspended in milli Q water. The zeta-potentials were measured to monitor the leasing of mPEG.

Assessment of *in vitro* cellular uptake of fMSNs nanoparticles by TEM and intracellular distribution of FITC- labeled fMSNs by flow cytometry and confocal microscopy

MDA-MB-231 cells were seeded in T-75 flask at a density of 2×106 cells/mL. Cells were treated with 400nM fMSNs prepared

in fresh DMEM at two different pH (6.8 and 7.4) for 24h. The cells were collected by centrifugation at 1200rpm for 3min, and the cell pellets were prefixed sequentially with 2.5% glutaraldehyde, 2% Para formaldehyde solution, and post-fixed with 1% osmium tetroxide followed by dehydration through a series of ethanol and infiltrated with resin. The resin sample blocks were trimmed, sectioned to electron-transparent ultrathin sections, and collected on carbon coated copper grids, and then double stained with uranyl acetate and lead citrate before viewing under the TEM. Intracellular uptake of FITC- labeled fMSNs can be detected both quantitatively and qualitatively by flow cytometry and co focal laser scanning microscopy (CLSM, And or Spinning Disc Confocal Microscope). Briefly, MDA-MB-231 cells were seeded in 60 mm dishes at a density of 2×1^{04} cells/mL and incubated for 24 h. The cell mono layers were washed twice with PBS and incubated with fresh cell culture medium containing FITC- labeled fMSNs at two different pH (6.8 and 7.4) for 60min to 16h at 37 °C in a 5% CO_2 atmosphere. Cells were then trypsinized and centrifuged at 1200 rpm for 3min, pre incubated with 0.25% Try pan blue for 1min to quench fluorescence of FITC-labeled fMSNs absorbed on the cell surface, washed and re-dispersed in 400μL PBS. The flow cytometry was performed with a FACS Scan Cytometer equipped with Cell Quest Software (BD Biosciences, San Jose, CA, USA) by counting 10,000 events, and data were reported as fold increase above control (cells without FITC-labeled fMSNs).

The results are expressed as the percentage of the mean of fluorescence intensity. Cells were seeded in confocal dishes at a density of 2×10^4 cells/mL and allowed to adhere for 24h in growth medium before exposure to fresh cell culture medium containing FITC- labeled fMSNs at two different pH (6.8 and 7.4) for 3h at 37 °C in a 5% CO_2 atmosphere. Cells were fixed in 3.7% formaldehyde in PBS, pH 7.4, for 15min at room temperature, permeabilized with 0.1% tritonX-100 in PBS and incubated in 1% bovine serum albumin (BSA) in PBS to block nonspecific staining. Cells were stained with Rhodamine-Phalloidin (a commercialistic selective stain) and with 4, 6-diamidino-2-phenylindole (DAPI), mounted with antifade mounting medium.

The dishes were viewed by CLSM (And or). To examine whether nanoparticles were transported to lysosomes, we have incubated MDA-MB-468 cells in growth medium containing FITC- labeled fMSNs for 3 h at 37 °C in a 5% CO_2 atmosphere, washed with PBS, fixed and permeabilized as described above. Cover slips were stained with Lyso Tracker Red (a commercially so some selective stain) and then mounted with anti-fade mounting medium. The slides were viewed by CLSM (And or).

In vitro Cytotoxicity Analysis

For Cytotoxicity study fresh blood from five healthy individuals was collected in heparin zed tubes and lymphocyte cultures were carried out for micronuclei analysis following the standard protocol of Migliore et al. [44]. This experiment was performed in accordance with the institutional ethics

committee's guidelines. Briefly, lymphocytes from 0.5mL whole blood was separated using ficoll-gradient centrifugation in Histopaque-1077 and cultured in RPMI-1640 at 37 °C for 72h followed by incubation with 400nM of NFT-fMSNs for another 48h. Standard dose of Mitomycin C (0.006mg) and Cyclophosphamide (0.1mM) were used as positive controls for chromosomal aberration and micronucleus (MN) formation assay respectively.

For chromosomal aberration study, 100ml colchicines (0.04%) was added in the culture 2h before and in case of MN formation, cytochalas in B (a cytokines is blocker) was added to each culture to give a final concentration of 6μg/ml 4h before harvesting the cells. After incubation, the cells were centrifuged at 1000rpm for 5min. Supernatant was discarded and cell pellets were treated with a weak hypotonic solution (0.075 M KCl/ saline, 1:9) for 5min. After centrifugation, the cells were fixed in fresh fixative (methanol/glacial acetic acid, 3:1).

Fixative was removed by centrifugation and two more changes of fixative were performed. The cells were dropped onto wet clean slides and the slides were air-dried and stained with 5% Giemsa in phosphate buffer (pH6.8). Finally, slides were examined randomly for deducing the mitotic index and scored for chromosomal aberrations at 100X. Data derived was expressed in percentage. At least 100 bi nucleated cells from each subject were examined for micronuclei under the microscope at 60X magnification.

Cell Viability Assay

Cell viability was also measured by 0.1% Try pan blue exclusion assay. Briefly, treated or untreated cells were assessed microscopically with a hemacytometer for dead cells by trepan blue exclusion. Cell viability was calculated by dividing the non-stained (viable) cell count by the total cell count. Results were expressed by averaging the number of cells in four squares and multiplying this average by the dilution factor.

Determination of percentage of cell viability by MTT assay

In vitro anti proliferative-cytotoxic activity was determined using MTT assay. Each breast carcinoma cell lines were harvested at the logarithmic growth phase and were seeded into 96-well plates at a density of 2500cells per well in 100μL DMEM growth media for 24h prior to treatment. Medium was replaced by fresh growth medium containing six different concentrations (100, 200, 400, 500, 750, 1000nM) of free and NFT- loaded fMSNs. After 24h and 48h incubation time, each well was treated with 20μL of MTT solution (5mg mL−1) and plates were incubated for 4h at 37 °C. Afterwards the medium was removed and plates were incubated for another 30min at 37 °C under gentle shaking with 100μL DMSO. The Formosan crystals were solubilized in DMSO, and the absorbance was determined at 570nm by using an automated computer-linked micro plate reader (Polar

star Optima, Germany). The percentage of cell viability was determined relative to non-treated cells to obtain the IC50 value.

Determination of cell cycle by flow Cytometry

Flow cytometry was performed to determine the effect of NFT- fMSNs on the cell cycle of MDA-MB-468cells. Propidium iodide (PI) was used to stain the DNA and Ribonucleic a (RNase A) for hydrolysis of phosphodiester bonds between the nucleotides. Briefly, 2×10^4 cells/mL MDA-MB-468 cells were seeded into six-well plate and incubated for overnight. After reaching ~75% confluency, the cells were treated with NFT- fMSNs at concentrations of 100, 250, 400, and 500nM for 24h. In separate experiments, MDA-MB-468cells were treated with 400nM NFT- fMSNs for 4, 8, 12, 24, and 48 h. Cells were trypsinized and fixed with chilled absolute methanol at -20 °C for 5mins and then incubated at 4 °C for 2-3h. The cells were then incubated with 50μg RNase A for 2h at 37 °C and subsequently incubated with 60μg PI at room temperature. Typically, a total of 10000 events were counted per sample for cell cycle analysis using a FACS Cali bur flow cytometer (Becton Dickinson Immune cytometry Systems, San Jose, CA, USA) and the percentage of cell cycle phases was quantified by Mod Fit LT software (Version 2.0, BD Biosciences).

Flow cytometry assay of cellular apoptosis by annex in V-FITC

Apoptosis was observed by Annex in V-FITC/PI staining assay, using FACS analysis, by counting 10,000events and data were evaluated using Cell Quest Software. In this experiment, MCF-7, MDAMB-231, MDAMB-468, 4T1, NIH/3T3, and MCF-10A cells were treated with NFT- fMSNs at their respective IC50 values for 24h. Cells were trypsinized and washed twice with cold PBS, and then re suspended in 1X binding buffer with 5μL annex in V-FITC and 5μL of propidium iodide at a concentration of 1×10^5 cells mL-1 in a total volume of 100μL. The cells were gently mixed and incubated in the dark for 15min at room temperature. Following that, 400μL of 1Xbinding buffer was added to each tube and then flow cytometric analysis was executed within 1h, followed by quadrant statistics analysis for necrotic and apoptotic (early and late) cell populations.

Measurement of intracellular ROS production

Intracellular ROS generation was checked using an oxidative-sensitive fluorescent probe2',7'-dichlorfluorescein-diacetate (H2DCFDA) by flow cytometry and CLSM. In brief, following treatment with 400nM of NFT- fMSNs for different pre-assigned time points (0, 2, 4, 6, 8, 10, 12h), cells were washed twice with PBS, incubated with 10μM H2DCFDA in a culture medium at 37 °C for 30min in dark and immediately analyzed Using CLSM as well as harvested for flow cytometry (BD Biosciences, CA, USA) with excitation at 488nm and emission at 530nm. ROS generation was measured by flow cytometry.

Measurement of mitochondrial membrane potential (ΔΨm) by JC-1

An alteration in mitochondrial membrane potential was analyzed by flow cytometry and CLSM using JC-1, surrogate marker extensively used to detect damages in ΔΨm. It is a cationic fluorescent dye, bearing a delocalized positive charge that accumulates as aggregates (red fluorescence) in polarized mitochondrial membranes of normal cells. In apoptotic cells, JC-1 accrues in the cytoplasm in monomeric form (green fluorescence) due to disruption of ΔΨm. MDA-MB-231 cells were cultured on cover slips for 24h, treated with 400nM of NFT- fMSNs for 0, 4, 8, 12, 16 h at 37 °C. Following this, cells were washed twice in cold PBS and incubated with 5μg/mL JC-1 at 37 °C for 30min. Subsequently, cells were washed and analyzed by CLSM (And or) at 63X. For flow cytometry, cells were harvested by centrifugation after treatment, suspended in PBS and incubated with 10μg/mL of JC1 at 37 °C for 15min, stained cells were washed, suspended in PBS and analyzed using FAC Scan Cytometer (BD Biosciences, CA, USA).

MPTP assay using calcein-AM

Mitochondrial permeability transition pore (MPTP) opening was assessed using the calcein-cobalt assay. Cells were cultured on glass bottom culture dishes with or without NFT-fMSNs (350nM) for 16h, washed and incubated with calcein AM (1μM) at 37 °C in the dark for 20min. Again cells were incubated for another 15min at 37 °C in the dark with $CoCl_2$ (1mM) and washed in 1X HBSS. Images of live control and treated cells were captured sequentially for calcein fluorescence (excitation: 488nm, emission range: 495-540nm) using a confocal microscope (And or).

Cytochrome c release study

Immune fluorescence technique was performed to assay cytochrome c release. MDA-MB-231 cells were seeded on cover slips, incubated at 37 °C in 5% CO_2 and treated with 400nM of NFT- fMSNs for 16h. The cover slips were incubated in culture medium containing 100nM MitoTracker Red at 37 °C for 30min, washed thrice in PBS, fixed with 3.7% formaldehyde for 10min at room temperature and permeabilized with 0.1% TritonX-100 for 15min on ice. Subsequent blocking in 1% BSA for 1h at room temperature, cells were incubated overnight with primary antibody against cytochrome c at 4 °C and then incubated again with Alexa Fluor 488-conjugated secondary antibody at room temperature for 1h. Finally, cover slips were washed with PBS, mounted on glass slides and examined under CLSM.

Assessment of DNA strand breaks by TUNEL assay

TUNEL assay was performed on NFT- fMSNs treated MDA-MB-231 cells to measure inter nucleosomal DNA strand breaks in apoptotic cells. Control and treated cells were fixed with 3.7% formaldehyde in PBS (pH 7.4) for 10min at room temperature. After multiple wash, cells were incubated using TUNEL reaction mixture (Roche) for 1 h at 37 °C according to manufacturer's instructions to detect apoptosis. The slides were mounted in Vectashield containing 100ng/ml DAPI and examined under CLSM.

Wound healing assay

For wound healing assay, $2 \times 10^{5\text{mL-1}}$ MDA-MB-231 cells were seeded in 12-well plates and incubated overnight at 37 °C. After reaching confluence, the monolayer was scratched straight with a sterile 10μL pipette tip and the culture medium was replaced with 1mL of fresh medium (containing two different concentrations of NFT- fMSNs and compared with DMEM alone). At the start of the experiment (t=0) and normally after 12, 24and 48h of incubation the plate was visualized under an optical microscope (Leica). Images were analyzed using Image J Software (National Institutes of Health, Bethesda, MD, USA) to reveal the distance of migration inMDA-MB-231 cells.

Confocal and scanning electron microscopy to determine the morphology and cytoskeletal dynamics of cells

The morphology of breast carcinoma cells were monitored under CLSM and FESEM. The cells were grown on poly-L-lysine coated glass cover-slip overnight at 37 °C in 5% CO_2. The cells were treated with specific dose of NFT-fMSNs and kept in the CO_2 incubator for overnight. Next day, the cells were washed with PBS, and then fixed with 2.5% glutaraldehyde buffered in PBS for 1h. Subsequently, the cells were washed with PBS and dehydrated through a series of different concentrations of alcohol (30, 50, 70, 85, 95 and 100%), and then subjected to air drying. The samples were visualized by FESEM (FEI Quanta 250, USA) immediately after gold coating. For CLSM analysis, the cells were fixed with 3.7% formaldehyde and permeabilized with 0.1% Triton X-100. Cells were incubated with Rhoda mine-conjugated phalloidin (Life Technologies) for 30min. The samples were mounted on clean glass slides and visualized under confocal microscope.

Protein extraction and western blot analysis

Proteins were extracted from control and treated cells in RIPA buffer (Thermo Scientific) supplemented with protease inhibitor cocktail (Roche, USA). Lysates were centrifuged at 12,000×g for 15min at 4 °C to remove cellular debris, and the concentration of total cellular protein was determined using BCA protein assay kit according to the manufacturer's instructions (Thermo Scientific), dissolved in SDS sample buffer and run on10-12% polyacrylamide gels, and followed by transfer to PVDF membranes by standard protocols. Membranes were probed with primary antibodies against Caspase 3 (1:500), Caspase 9 (1:500), Bax (1:500), Bcl-2(1:500), Cleaved PARP (1:500), IL-6 (1:500), IL-6R (1:500), P-gp-130 (1:500), P-STAT 3 (1:500), P-Akt (1:500) and β-actins (1:1000) at 4 °C for overnight. Incubation with the primary antibody was pursued by incubation with

horse radish peroxidase-linked respective secondary antibodies for 1h at room temperature, following which; the membranes were washed again three times before being developed under enhanced chemiluminescence condition. The membranes were viewed using the Chemi Doc™ MP (Bio-Rad). β -actins was used as protein loading control.

Fluorescence immune cytochemistry study

For Immune fluorescence study, control and treated MDA-MB-231 cells were grown on glass cover slips, fixed with 3.7% formaldehyde and permeabilized with 0.1% Triton X-100. Cells were then incubated sequentially with 1% BSA in phosphate buffered saline with 0.1% tween 20 (PBST), primary antibody (diluted according to manufacturer's protocol) at 4 °C for overnight. After repeated washing with PBST, the cover slips were incubated with TRITC-conjugated respective secondary antibody (Sigma) for 1 h at room temperature followed by nucleus staining with DAPI (Nitrogen, Carlsbad, CA). The samples were mounted on clean glass slides and visualized under CLSM.

In silico IL-6R binding study

Molecular docking is an essential tool to identify the bioactive molecule which predicts the interaction pattern between receptors and ligands. The high resolution crystal structure of the IL-6R (PDB code: 1N26) [45,46] was downloaded from RCSB protein data bank for docking study. According to Unipart (P08887), it is found that the binding site of crystal structure is situated in residues 94 to 194. We have docked the proposed drug molecule (ligand) at the classical cytokine-binding domain containing these amino-acid residues. We have also considered the carbohydrate molecules attached at the sites on the faces of the receptor during docking because these carbohydrate molecules are directly involved in either the binding of IL-6 or the formation of the signaling complex with gp130.

The docking study was performed using Ligand Fit module of receptor-ligand interactions protocol section available in Discovery Studio 2.1 (San Diego, CA, USA.). All the duplicate structures were removed in case of ligand preparation. The parameter, options for ionization change, tautomer generation, isomer generation and three-dimensional generator were set to true. Thus, the protein molecule prepared was defined as the total receptor and the binding site was generated using the option 'find sites from receptor cavities' available in Discovery studio 2.1. The ligand was docked into the binding site of the receptor and the binding energies (dock score) were calculated between ligand and the receptor.

PLP1 energy grid was chosen for docking study. Prior to docking, the conformational search of the ligand was performed by Monte Carlo trial method. Maximum internal energy was set

at 10000 Cal and pose saving with interaction filters were set as default. 50 poses were saved for each compound. The 50 docked poses were ranked based on the dock score (based on LigScore1, LigScore2, PLP1, PLP2, Jain and PMF) [Discovery Studio 2.1, San Diego, CA, USA.] function. Finally, the interaction pattern was analyzed.

In vivo study

Animal maintenance and breast tumor model

Female BALB/c (3-4 weeks old, 16-18 gm) mice used in this experiment were maintained in a well ventilated animal house with 12 h light-12 h dark cycle. The animals were fed with standard laboratory feed and water ad labium. All experiments were performed as per the guidelines and as recommended by the Institutional Animal Ethics Committee (IAEC) (Bose Institute, Kolkata, India) (Approval No. IAEC/BI/06/2011). Female BALB/c mice were challenged with 1×106 cells/0.1mL/mice 4 T1 cells subcutaneously into mammary fat pad to form primary tumor. After the tumor volume reached 70-100 mm^3, animals were randomly divided into three groups. There were five mice in each group. The tumor-bearing mice were treated with normal saline, free NFT (2.5mg/kg body weight), and NFT-fMSNs (equivalent dose of NFT, 2.5mg/kg body weight) by tail vein injection every 4th day for 28 days. Body weight of mice was detected as an index of toxicity. Tumor size was measured every seven days with a caliper and calculated using the following Formula 4:

$$\text{Tumor weight} \left(gm \right) = \left(a \times b^2 \right) \text{.......... (4)}$$

Where 'a' is the largest and 'b' is the smallest diameter of the tumor.

In vivo toxicity assessment of fMSNs and NFT- fMSNs

The mice were randomly divided into four groups: fMSNs free NFT, NFT- fMSNs and saline control group. We used five mice per group as this number has sufficient statistical power to examine the differences in the toxic responses. We used 0.5-20mg/kg body weight particles for intravenous injection through tail vein twice a week for 4 weeks. Animal weights were monitored following nanoparticle injections and were sacrificed after 7days of last dose to obtain blood and organs. Blood biochemistry of liver and kidney panels was analyzed.

Histology of Major Organs

The major organs (liver, kidney, lungs, spleen and heart) from the euthanized control and NFT- fMSNs treated mice were collected on day 35. Then the formalin-fixed paraffin-embedded tissues were cut into 3-5μm-thick sections. The sections were stained with hematoxylin-eosin and examined by light microscopy (Leica).

Biodistribution of fMSNs in Mice

Ex vivo biodistribution study by fluorescence imaging

FITC was incorporated into fMSNs to track the nanocarriers in mice bodies. The size of our FITC incorporated fMSNs (FMSNs) was 100-130nm (as determined by DLS), and we expected that FMSNs would preferentially accumulate in tumors through the EPR effect and folate receptor that is up-regulated in breast cancer. The FMSNs were suspended in 500μL of PBS, pH 7.4 and injected via tail vein. The animals were anesthetized with required amount of urethane and sacrificed at pre-determined time points (4, 8, 12, 24, 48, 72and 96h). The organs (heart, kidney, liver, lung, spleen and tumor) collected from the mice were imaged in Kodak Image Station 4000 MM PRO.

In vivo biodistribution study by inductively coupled plasma-optical emission spectrometry (ICP-OES)

The vital organs (liver, kidney, spleen, heart, lungs and tumor) were collected for inductively coupled plasma optical emission spectroscopy (ICP-OES) to estimate the concentration of Si in order to check the biodistribution of this element in each organ. At 4, 24, and 48h post-administration (intravenous), each group was separately analyzed for tissue Si content. For this analysis, the animals were sacrificed after collection of blood, and the desired organs were weighed and digested with ultrapure nitric acid (1.00mL, 70%) by heating, diluted with deionized water and used for silicon determination using ICP-OES (Varian Vista-MPX, USA). All samples were analyzed in triplicate for the presence of silicon.

In vivo internalization study

Breast tumor tissues excised from the control and treated mice were washed in PBS and prepared for TEM analysis as previously described.

TUNEL and PCNA assay

Vehicle control and 5mg/kg body weight of NFT- fMSNs treated mice were sacrificed after 35 days. Tumors were excised and 8μm thick non-consecutive sections were obtained. Sections were deparaffinised, re-hydrated in graded alcohol, washed in PBS, permeabilized with 0.1% Triton X-100 for 15min on ice, blocked with 1% BSA in PBST for one hour at room temperature and were stained with Fluorescein-dUTP overnight at 4 °C. Sections were counter stained with DAPI and images were obtained at 60X in CLSM (And or). Immune-staining on mouse tumor tissue section for proliferating cell nuclear antigen (PCNA) was executed using biotinylated monoclonal Anti-PCNA primary antibody, biotin-conjugated secondary antibody and the signals were visualized with peroxidase-diamino-benzidine with subsequent counter staining using haematoxylin.

Estimation of biochemical serum markers

The serum was obtained by centrifuging the whole blood at 3000 rpm for 15min and the collected serum was submitted for biochemical analysis. The biochemical parameters - alanine aminotransferase (ALT), aspirate aminotransferase (AST) and alkaline phosphatase (ALP), creatinine (CREAT), blood urea nitrogen (BUN) were assessed using commercial kits (Abcam) following manufacturer's protocol.

Assessment of gelatinizes (MMP-2/9) by gelatin zymography

The expressions of activated MMPs (MMP-2/9) were analyzed by gelatin zymography. Samples were incubated for 30min at 25 °C in presence of 2% SDS and loaded onto an SDS-polyacrylamide gel containing 0.1% (w/v) gelatin (Sigma-Aldrich, St. Louis, MO) and subjected to electrophoresis. Following electrophoresis, the gel was washed with 2.5% Triton X-100 to remove SDS. Following this, the gels were incubated in 50mM Tris/HCL buffer, pH 7.5, containing 5mM $CaCl_2$, 1 μM $ZnCl_2$, 60mM NaN3 and 1% (v/v) Triton X-100 for 24 h at 37 °C. Gels were stained with 0.1% Coomassie Brilliant Blue R-250 (Sigma-Aldrich) for 1h and washed with distaining solution 7% (v/v) acetic acid until clear bands against an intensely stained background appeared. Gelatin degradation was revealed as clear bands in a dark field.

Lung metastasis study

For lung metastasis study, 5×10^5 viable 4T1 cells were re suspended in PBS and injected into the lateral tail vein of mice in a volume of 100μL. Mice were randomly divided into 2 groups (5 mice per group): (i) vehicle control group, (ii) NFT-fMSNs dose group (i.v. dose of 2.5mg/kg body weight). Dose administration was performed via tail vein from the 8th day following tumor implantation in every 3rd day for 22 days.
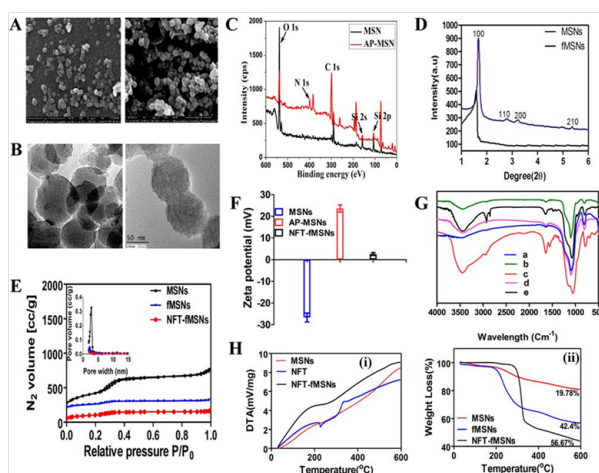
Statistical analysis

All graphical readings shown were performed in triplicates and values expressed as the mean ± S.D.

Results were considered statistically significant when p≤0.05.

Results

Physico-Chemical Characterization

Scheme 1: Schematic diagram depicting the overall synthetic approach used in the preparation of NFT-fMSNs for this study.

Figure 1: (A) FESEM and (B) TEM images of bare (left side) and surface functionalized drug containing MSNs (right side). (C) Wide-scan XPS spectra of bare (black line) and APTES-functionalized (red line) mesoporous silica nanoparticles.(D)SXRD patterns of bare and surface functionalized MSNs.(E)Nitrogen adsorption desorption isotherm and pore width distribution of MSNs, fMSNs and NFT-fMSNs. (F) Values of zeta potential of MSNs, AP-MSNs and NFT-fMSNs at pH 7.4. (G) FTIR spectra of (a) as synthesized MSNs, (b) APTES-functionalized MSNs, (c) CBA-functionalized MSNs, (d) β-CD-functionalized MSNs and (e) fMSNs. (H) (i) DTA and (ii) TGA curves of MSNs, fMSNs and NFT-fMSNs.

The NMR spectrum of nifetepimine was taken by dissolving the sample in DMSO-d6. [1H NMR: δ 1.08(3H, t, J = 7.1 Hz, -CH$_2$CH$_3$), 2.26 (3H, s,-CH$_3$), 3.98 (2H, m, -CH$_2$CH$_3$), 5.29 (1H, d, J = 3.3 Hz, CH), 7.63-7.69(2H, m, ArH), 7.87 (1H, s, NH), 8.07 (1H, t, J = 1.8 Hz, ArH), 8.11-8.13 (1H, m, ArH), 9.34 (1H, s, NH)]. Fourier Transform Infrared Spectroscopy shows characteristic peaks at 686.0, 693.0, 1088.4, 1224.3, 1346.5, 1525.9, 1629.8, 1688.7, 1708.6, 2821.3, 2964.2, 3100.0, 3217.7, 3329.5 cm^{-1}. Scheme 1 depicts the overall Synthetic approach used in this preparation. The scheme begins with the preparation of amine functionalized MSNs (AP-MSNs) and subsequently modified with 4-carboxyphenylboronic acid for anchoring β-cyclodextrin (β-CD) onto MSNs with a pH responsive boronic acid-catechol ester bond (pH 5.0) (Figure S1a) (Figure S1b).

Afterwards, NFT molecules were encapsulated into the hydrophobic core of the mesopores of MSNs. PEGylation and folic acid incorporation was performed by mPEG functionalized with adamantine (Ada) (mPEG-Ada), and Ada unit functionalized with foliate unit (FA-Ada). Finally, a mixture (1:1) of mPEG-Ada and FA-Ada was immobilized onto the surface of BA-MSN-DHPA-β-CD through Ada/ β-CD complexation. Here, mPEG shielding could effectively improve biocompatibility, water dispensability and suppress non-specific protein adsorption of the nanoformulations. FA was incorporated in order to impart the targeting specificity towards selected breast cancer cell lines. β-CD molecules have been used as gate keepers to control the release of NFT molecules from the pores of MSNs. Field emission scanning electron microscopy (FESEM) and transmission electron microscopy (TEM) images displayed a spherical particle diameter of 80 ± 10 nm, along with mesoporous nature of the synthesized MSNs (Figure 1A& B), left side).

Both empty MSNs and NFT-fMSNs displayed similar spherical morphology and average diameter Figure 1A & B, right side. However, the later does not show porous structure indicating entrapment of NFT molecules into mesopores and also display conjugations of the functional molecules. The introduction of 3-aminopropyltriethoxysilane (APTES) into MSNs was indicated by X-ray photoelectron spectroscopy (XPS). XPS elemental analysis also showed significant increase of nitrogen content in AP-MSNs surfaces Figure 1C, red line as compared to the original MSNs Figure 1C, black line. The existence of amino groups is important for further fictionalization of the nano particles through chemical modification. Then, the mesoporous characteristic of MSN was confirmed by small-angle X-ray diffraction (SAXRD) and Nitrogen adsorption–desorption isotherms.

The SAXRD pattern shows a sharp XRD reflection peak (100) with three other peaks associated with (110), (200) and (210) diffraction planes, indicating the formation of a well ordered mesoporous silica network Figure 1D. However, while compared with the XRD of empty MSNs, a lower contrast and slight deviation in the (100) value was observed in fMSNs indicating presence of covalent linkage of organic functional groups on MSNs surface. Nitrogen adsorption–desorption isotherms of MSN samples and their corresponding pore size distributions were studied according to the Brunauer-Emmett-Teller (BET) and Barrett-Joyner-Halenda (BJH)procedures Figure 1E.

Table 1: Properties of MSNs before and after NFT loading from N_2 adsorption– desorption isotherms. The surface area (S_{BET}), pore size (W_{BJH}) and pore volume (V_t) were measured using Brunauer-Emmett-Teller (BET) and Barrett-Joyner-Halenda (BJH) methods.

Samples	S_{BET} (m^2g^{-1})	V_t (cm^3g^{-1})	W_{BJH} (nm)
MSNs	1031	0.75	2.98
fMSNs	382	0.24	--
NFT-MSNs	253	0.18	--

The results showed that BET specific surface area (SBET), total pore volume (Vt) and BJH pore diameter (WBJH) were reduced in fMSNs and NFT-fMSNs due to loading of NFT molecules into the pores of the MSNs and surface fictionalization Table 1. As depicted in Figure 1E, the samples show type IV sorption isotherms of mesoporous materials with uniform pore size distributions and the inflection of the capillary condensation observed over a range of relative pressure (P/P0=0.3-0.5) that was evident from the presence of mesopores. It can be observed that all the MSN samples retain high SBET and Vt, indicating its possible application as a DDS.

Step wise fictionalization was observed via zeta potential, and Fourier transform infrared (FTIR) spectroscopy Figure 1F,G. The zeta potential (ζ) was monitored at each step of the synthesis. At pH 7.4, zeta potential of MSNs was around -26.7 mV but, after surface fictionalization with APTES, the value became positive (+23.4mV) due to the presence of amino groups. Finally, ζ value of the NFT-fMSNs was reduced to an almost neutral value (+2.3mV) due to mPEG shielding and FA anchoring onto the surfaces of fMSNs Figure 1F. Stability of the nanoformulations was checked at physiological pH and the result was depicted in Figure S2.
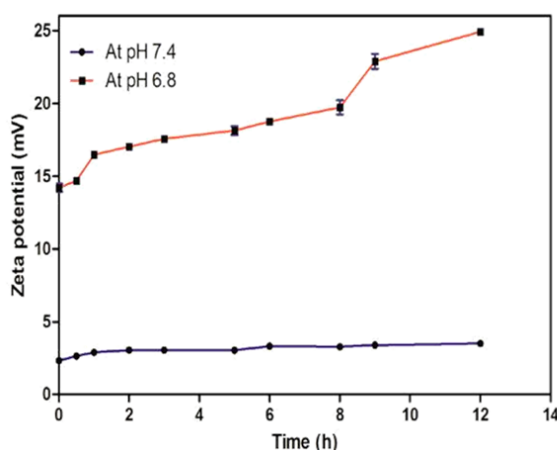

Figure S2: Zeta-potential measurements to study dissociation of mPEG from the surface of MSNs at two different pH.

Moreover, the zeta-potential values of NFT- fMSNs samples kept at 37 °C in PBS at different pH values for different times provide an indirect measurement of releasing of mPEG from the surface of MSNs. Zeta-potential values of the nanoformulations at pH 7.4 remained in the range of +2.3 mV to +3.55 mV within 12h. Nonetheless, the zeta-potentials of the nanoformulations, at pH 6.8, increased up to +13.7 mV within 45min and promoted to increase to +25.2 mV within 12h. These results demonstrated that the DDS was stable at physiological pH. All these features would increase circulation time of the nanoformulations for *in vivo* applications. Figure 1G illustrates the FTIR spectra of all samples in the range of 500-4000 cm^{-1} to study the organic functionalities on the surface of various MSNs.

The FTIR spectrum of MSNs Figure 1G, a shows typical bands attributed to Si-O-Sib ending (467 cm^{-1}), Si-O-Si symmetric stretching (805 cm^{-1}), external Si-OH groups (963 cm^{-1}), Si-O-Si asymmetric stretching (1077 cm^{-1}). The band at 1634 cm^{-1} adsorbed water molecules and -OH stretching at (3437 cm^{-1} reveals the presence of O-H bending vibration of).

A wide absorption band appearing in the range 3200-3500cm^{-1} indicates the existence of silanol groups in the MSNs. After modification with APTES, AP-MSNs displayed new peaks at 798, 1553 and 1634 cm^{-1}, which indicate the presence of N-H stretching vibration mode attributed to the amino groups of 3-aminopropyl groups grafted on fMSNs (Figure 1G, b).

After modification with 4-carboxyphenylboronic acid, a new band of 1378cm^{-1} was ascribed to the B-O bond. The peaks at 1457, 1474 and 3075cm^{-1} were assigned to the skeletal stretching vibrations of phenyl group bend with the CH2 bending and stretching vibrations due to 4-carboxyphenylboronic acid Figure 1G, c. After subsequent grafting with β-CD, the band at 1449, 2929 and 2958cm^{-1} were assigned to the stretching of –CH2 units of β-CD Figure 1G, d confirming β-CD grafting to the AP-MSNs. The adamantine (Ada) component was inserted into the cavity of β-CD on the MSNs surface via inclusion complexation and served as an anchor for the folic acid (Ada-FA) and mPEG (Ada-mPEG) moieties.

The bands at 819 and 2915cm^{-1} due to the –CH2 groups derived from mPEG and the bending vibration of C-H derived from phenyl groups in Ada-mPEG functional molecule, which further reflecting that Ada-mPEG was grafted onto the MSNs surfaces. FTIR spectrum of NFT-fMSNs shows characteristic peaks related to stretching frequency of the pyridine ring and p-amino benzoic acid of FA in the range of 1473-1649cm^{-1}. The peak at 3414cm^{-1} belongs to stretching vibration of N-H bond in primary amines and amide linkages. The line broadening appeared between 1657cm^{-1} to 1233cm^{-1} is pointing to the covalent linkage of FA with Ada.

The peaks observed in the FTIR spectrum for free NFT molecules were also observed in the spectrum for the NFT-fMSNs, proving the presence of NFT molecules Figure 1G, e. Differential thermal analysis (DTA) of free NFT, empty fMSNs and NFT-fMSNs are presented in Figure 1H (i). The thermo gram of free NFT shows an intense endothermic peak at 230 °C which corresponds to its intrinsic melting point. However, no endothermic peak has been observed in case of NFT-fMSNs, because NFT molecules have been successfully entrapped into the pores and due to complete coverage of the MSN surfaces by the bio-polymers. In thermo gravimetric analysis (TGA), the overall amount of drug loading can be detected by calculating weight loss. As shown in Figure 1H (ii), the loading fractions in all cases were estimated from the weight loss to the total initial weight. The weight loss of empty fMSNs and NFT-fMSNs has been found to be 42.4% and 56.67%, respectively. These results, together with the changes of particle size, zeta potential, thermo gravimetric analysis and FTIR spectroscopy demonstrated that fMSNs could be efficiently loaded with NFT, gated with β-CD and pH sensitive linkages, and also be PEGylated on the surface.

In vitro pH-dependent release of NFT from NFT-fMSNs

Three different pH values (7.4, 6.8 & 5.0) were chosen to mimic the normal plasma, tumor microenvironment and intracellular endosome to study accumulative NFT release from NFT-fMSNs in vitro. As shown in Figure 2A, at pH 7.4, NFT was barely released from NFT-fMSNs during specific time period (11%), which ensures effective pore capping by β-CD/Ada conjugate. However, under mild acidic environment (pH 6.8) sustained release of NFT occurred at a marginally higher rate than that at pH 7.4. Furthermore, when suspended at pH 5.0, NFT molecules were released from NFT-fMSNs at a comparatively much higher rate, illustrating the efficacy of the designed acid-responsive release mechanism.
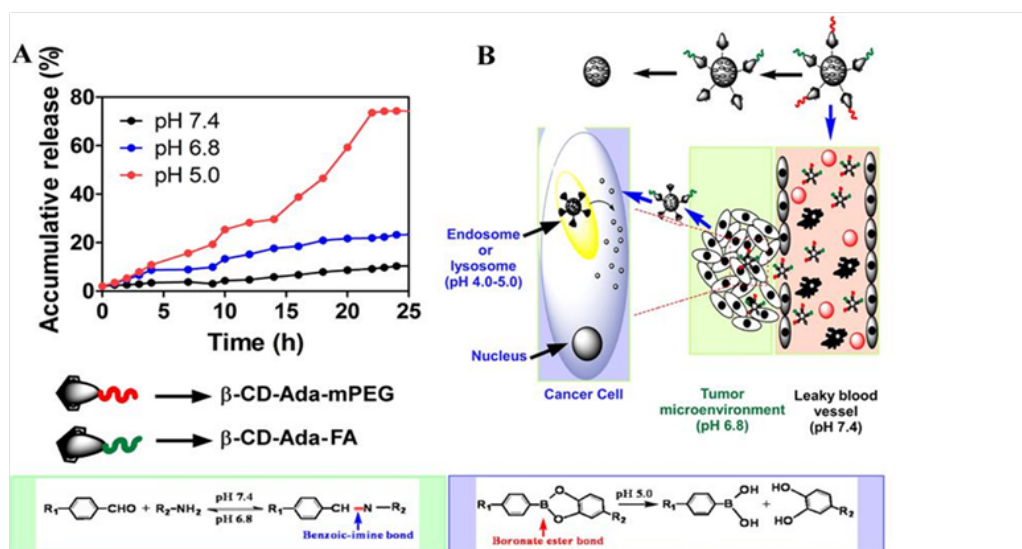

Figure 2: (A) pH triggered drug release profiles of NFT-fMSNs under three different pH. (B) Schematic illustration of NFT molecule release from gated NFT-fMSN nanoplatform in vivo with pH-responsive drug release property at pH 6.8 and pH 5.0.

This finding indicates that the boronic acid-catecholester bonds were stable at pH 7.4 and a relatively small fraction of cleavage of these linkers occurred in the tumor microenvironment (pH 6.8). However, when exposed to endosomal pH, most of the linkers were cleaved, leading to β-CD dissociation, unblocking of the nanotunnels and eventually release of NFT molecules into cytoplasm Figure 2B. The pH-sensitive benzoic-imine linkages were stable at physiological pH because of the proper π-π conjugation. Under weak acidic tumor extracellular pH (~6.8), these linkages begin partially hydrolyzing to accelerate mPEG release and to facilitate internalization of the MSNs. Thus, this new pH-responsive mesoporous nonmaterial could achieve on demand release of anticancer drugs exhibiting its wide applicability and even great potential for tumor therapy in response to cascade pH stimuli within tumor microenvironment.

In vitro cellular uptake and endosomal/lysosomal escape

MDA-MB-231 cells were treated with FITC-labeled fMSNs (FITC-fMSNs) at two different pH values, 6.8 and 7.4. As detected by Fluorescence activated cell sorting (FACS, FACS Cali bur flow

cytometer, BD Biosciences, SanJose, CA, USA) in a time-dependent manner, internalization of FITC-fMSNs occurred within 45min after treatment and substantially accumulated during the first two-hour of incubation Figure 3A. These results were further validated by Confocal laser scanning microscopic (CLSM, And or) examinations. Following incubation for 6h, cellular internalization of FITC-fMSNs, displayed by green fluorescent aggregates, at pH 6.8 was significantly higher than that at pH 7.4 Figure 3B & C, a-e. Transmission electron microscopic (TEM) images supported by energy-dispersive X-ray spectroscopy

(EDX) Figure 3D, a-c of both control and empty fMSNs treated MDA-MB-231cells showed distinct cell membrane and intact nuclei, demonstrating that fMSNs internalization did not affect cell viability and proliferation. Compartmentalization of FITC-fMSNs into lysosomes of MDA-MB-231 cells, assessed by CLSM using Lysotracker Red also complimented the results. Figure S 3A (upper panel) shows that after 4h of incubation, FITC-fMSNs were localized (yellow spots) within acidic organelles (endoscope/lysosome).
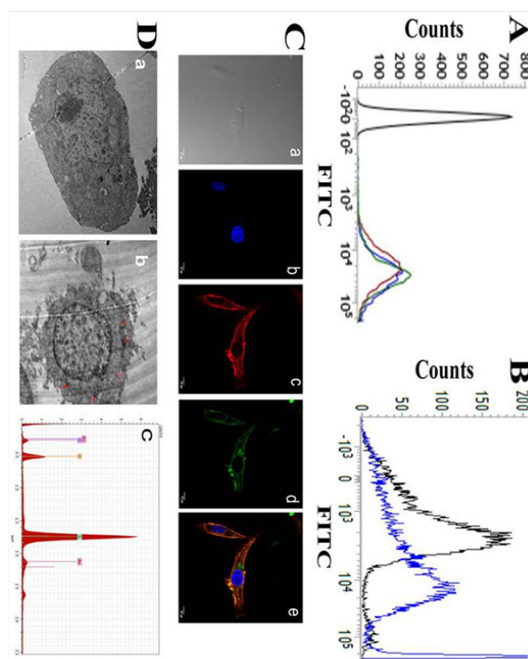
Figure 3: (A) In vitro cellular uptake of FITC-fMSNs in MDA-MB-231 cells analyzed by FACS (Black line- controlcells, red, blue and green lines are cells treated for 45 min, 2 and 6 h respectively with FITC-fMSNs), (B) FACSdata showing better internalization of FITC-fMSNs at pH 6.8 (blue line) than that of at pH 7.4 (black line) at 6h. (C) CLSM images of MDA-MB-231 cells after incubation for 6 h with FITC-fMSNs. (a) DIC, (b) DAPI, (c) Rhodamine-Phalloidin, (d) FITC-fMSNs, and (e) merged images. (D) TEM images of cross sections of MDA-MB-231 cells (a) untreated, (b) treated with fMSNs showed healthy cellular morphology. Tiny spherical particles of fMSNs (indicated by red arrows) were noticed inside the treated cells, (c) spot EDX image showing internalization of fMSNs within treated MDA-MB-231 cells.

Moreover, after 12h, most of the FITC-fMSNs were succeeded endosomal escape via endosome buffering" effect and were distributed into the cytoplasm Figure S 3A, lower panel due to hydrolysis of boronic acid-catecholester bond at pH 4.5-6.0 followed by gate keeper dissociation. So, it is important to note that this acid-responsive nanocarriers not only works in simulated endosomal pH but also effective in the cellular systems. In order to justify the usefulness of FA molecules as targeting ligand, FACS was performed to figure out the cellular uptake of FITC-fMSNs by FR-positive human cervical carcinoma (HeLa) cells and FR-negative human embryonic kidney (HEK 293) epithelial cells.

The resultant data were summarized in Figure S3 B-D. The cellular uptake of FITC- fMSNs by FR-positive HeLa cells cultured in an FA-free cell culture medium and FR-negative HEK 293 epithelial cells cultured in a normal cell culture medium were evaluated by FACS. Figure S3 B (Left side) demonstrated a strong green fluorescence from HeLa cells, while no noticeable fluorescence was observed from HEK 293 cells Figure S3 B, right side after incubation with FITC- fMSNs for 6h. In order to confirm folate-mediated endocytosis HeLa cells were incubated with FITC-labeled MSNs coated with mPEG-Ada and Ada-FA (1:1 molar ratio), and FITC-labeled MSNs coated only with mPEG-Ada.
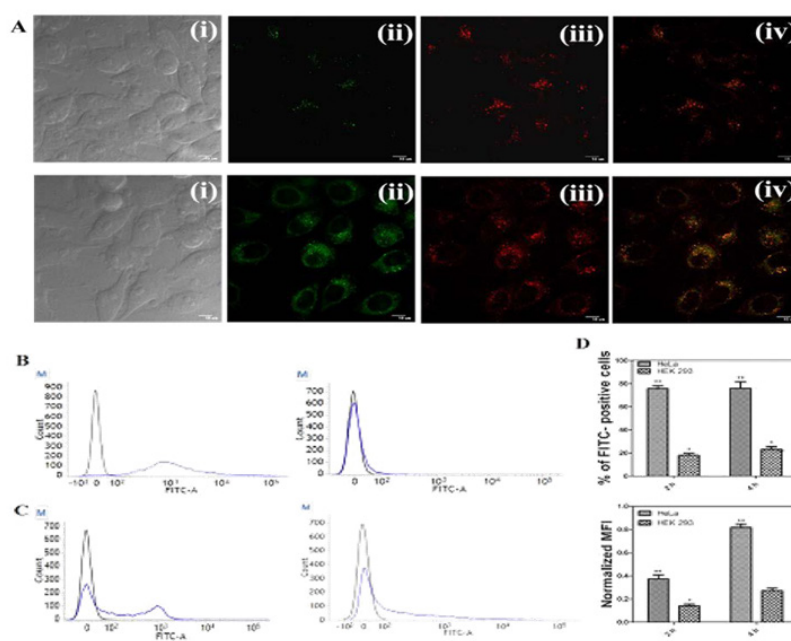
Figure S3: (A) Confocal images of MDA-MB-231 cells treated with FITC- fMSNs for 4 h (Upper panel) andfor 12 h (Lower panel). Lysotracker red was used to stain the acidic organelles of the cell. (i)DIC image and cells were stained with (ii) FITC- fMSNs, (iii) Lysotracker red, and (iv) merged images. Scale bar: 10µM. Flow cytometry analyses showing FR- mediated endocytosis. (B) Folate receptor over-expressed on HeLacells uptake FITC-labeled fMSNs more than HEK 293 cells, (C) HeLa cells incubated with FITC-labeled MSNscoated with mPEG-Ada and Ada-FA endocytosed more than FITC-labeled MSNs coated with mPEG-Ada. (D) Bar diagram shows % of FITC positive cells and MFIs of the cells after 2 and 4 h of incubation with FITC-labeled MSNs.

A strong green fluorescence was observed from HeLa cells incubated with FITC-labeled MSNs coated with mPEG-Ada and Ada-FA Figure S3 C, left side, while HeLa cells incubated with FITC-labeled MSNs coated only with mPEG-Ada showed insignificant green fluorescence proving FR-mediated endocytosis Figure S3 C, right side of NFT-fMSNs. Figure S3 D shows almost 80% of the HeLa cells and about 23% HEK 293 cells were FITC positive after 2 and 4h of incubation with FITC-labeled MSNs.

Only minor differences were observed between these two time points indicating most of the nanoparticles were internalized within 2h. The mean fluorescence intensities (MFIs) of the cells after 2 and 4h of incubation with FITC-labeled MSNs for both the cell lines indicate MFI of HeLa cells is about five times higher than that of HEK 293 cells Figure S3 D. The MFI should be directly correlated with the mean number of particles taken up per cell and these results give further proof that FA can be used as an efficient targeting ligand.

Anticancer efficacy of NFT-fMSNs

In vitro cytotoxic effects of free NFT, empty fMSNs and NFT-fMSNs (50-1000nM) on MDA-MB-231,MDA-MB-468, 4T1, NIH/3T3 and MCF-10A cell lines for 24h was investigated using MTT assay. A dose dependent reduction of cell viability was observed at 24h post-treatment with NFT-fMSNs Figure 4A. Potency of cell growth inhibition of different formulations was expressed through their IC_{50} values. Table 2 depicts a significantly lower IC50 value of NFT-fMSNs as compared to that of free NFT (35-45µM) or empty fMSNs (>50µM). Therefore, it can be emphasized that treatment of breast cancer cells with NFT-fMSNs augmented inhibition of cancer cell proliferation and survival.

Table 2: Comparison of the IC_{50} values (in nM) for fMSNs, NFT and NFT-fMSNs against breast cancer and normal cell lines as determined using MTT assay.*MCF7, MDA-MB-231 and MDA-MB-468, human breast adenocarcinoma; 4T1, mice breast tumor cells; NIH/3T3, mouse murine embryonic fibroblast; MCF-10A, non-cancerous human breast cells.

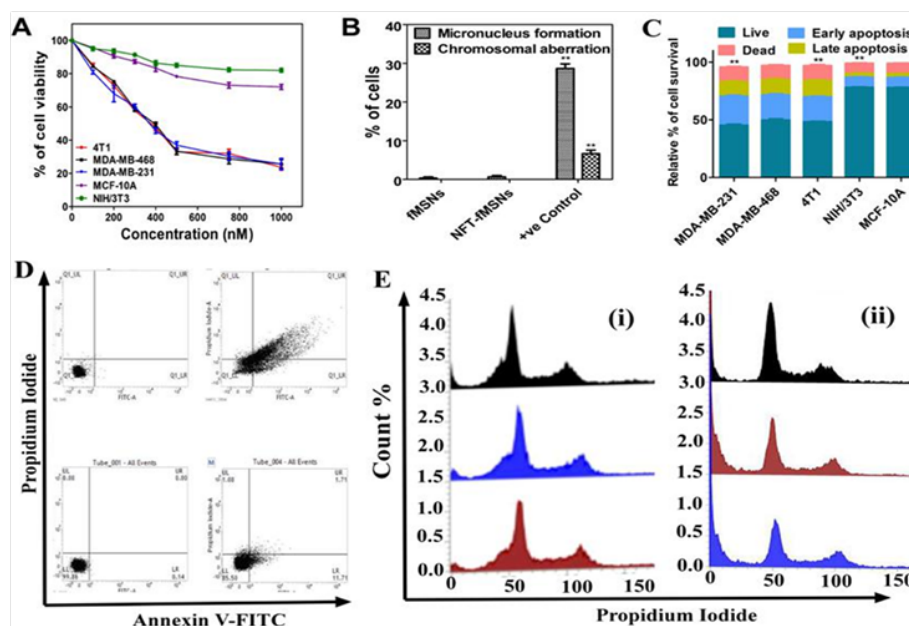| Treatments	*Cell Lines					
(IC_{50} nM)	MCF 7	MDA-MB-231	MDA-MB-468	4T1	NIH/3T3	MCF-10A
fMSNs	>50000	>50000	>50000	>50000	>50000	>50000
NFT	45000	42000	38000	35000	>50000	>50000
NFT-fMSNs	~ 450	~ 400	~ 400	~ 350	>1000	>1000

Figure 4. (A) Cell viability analysis of NFT-fMSNs at different concentrations ranging between 0 and 1 μM using MTT assay. Data generated from three independent experiments. (B) The graph shows % of micro-nuclei formation and chromosomal aberration in human peripheral lymphocytes after 72h of NFT-fMSNs treatment. (C) Stacked bars exhibit the relative % of cells treated with NFT-fMSNs at their respective IC50 values those are viable, early apoptotic, late apoptotic or dead phase. (D) Representative FACS images of NIH/3T3 cells (lower panel) display no significant effect of NFT-fMSNs on cell viability whereas MDA-MB-231 cells (upper panel) displayed significant apoptosis when treated with NFT-fMSNs at the same concentration as analyzed by Annexin V-FITC and propidium iodide (PI) assay. (E) Cell cycle phase distribution of nuclear DNA was determined by FACS. (i) Upper panel: control cells; middle and lower panels: NIH/3T3 cells treated for 8h, 18 h and 24 h with NFT-fMSNs. (ii) Upper panel: control, middle and lower panels: MDA-MB-231 cells treated for 18 h and 24 h with NFT-fMSNs. Graphs display DNA content (x-axis) versus counts (y-axis).

Furthermore, in order to validate the cytotoxic potential of NFT-fMSNs, chromosomal aberration and micronuclei (MN) formation were checked in human peripheral lymphocytes treated with NFT-fMSNs (500nM) for 72h. Our results indicate that treatment with NFT-fMSNs resulted in absence of micronuclei incidence and chromosomal aberration Figure 4B. This observation is in agreement with the fact that NFT-fMSNs pose no significant toxicity towards normal cells.

NFT-fMSNs induced cell apoptosis and the pathways involved

To investigate whether the cytotoxicity of NFT-fMSNs at 24hours was caused by apoptosis on MDA-MB-231, MDA-MB-468, 4T1, MCF-10A and NIH/3T3 cell lines, the number of apoptotic cells was measured using Annex in V-FITC/PI staining. No significant level of apoptosis was observed on normal cell lines (MCF-10A and NIH/3T3) with 80% cells being alive following NFT-fMSNs (400nM) treatment for 24h where as marked apoptosis was evident on the breast cancer cells when treated with NFT-fMSNs at the same concentration Figure 4C & D. Cell cycle analysis by FACS showed that NIH/3T3 cells treated with of NFT-fMSNs (400nM) for 24h did not lead to a change in cell cycle distribution or have no significant effect on cell apoptosis suggesting NFT-fMSNs did not disrupt the normal cellular growth of NIH/3T3 cells Figure 4E, (i).

However, results of PI staining indicates significant change in sub G0 population of MDA-MB-231 cells, which indicates increase in the number of apoptotic cells in 400nM treated NFT-fMSNs. Initial apoptotic cell percentage was ~11% in 8h which increased to ~39% and ~46% in 18 and 24h subsequently Figure 4E, (ii). To assess the role of mitochondria in NFT-fMSNs-induced cell apoptotic death, we tested whether NFT-fMSNs caused a loss of the mitochondrial membrane potential (ΔΨ m) of the breast cancer cells by staining with the met achromatic fluorescent probe JC-1.

Cytometry- and confocal microscopy-based analyses showed prominent fluorochrome accumulatation in polarized mitochondria, exhibiting heterogeneous staining pattern of red and green fluorescence in control MDA-MB-231 cells whereas a sharp decrease in red fluorescence and subsequent increase in green fluorescence was observed in cells treated with NFT-fMSNs for 16 h Figure 5A.

FACS data also revealed no impressive alteration in ΔΨ m of NIH/3T3 cells whereas significant changes were recorded in MDA-MB-231 cells treated with NFT-fMSNs for 16 h Figure S4 A & B. Furthermore, Figure S4 C illustrates that ΔΨ m disintegration promotes abrupt increase in permeability of the inner membrane with formation of NFT-fMSNs induced nonspecific mitochondrial permeability transition pores (MPTPs) that is traditionally linked to mitochondrial dysfunction, ultimately leading to cell death. ΔΨ m disruption and subsequent cell apoptosis is always associated with intracellular generation of reactive oxygen species (ROS).
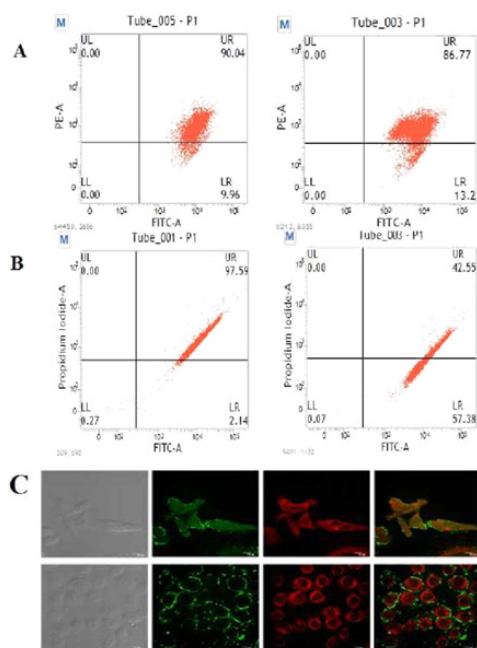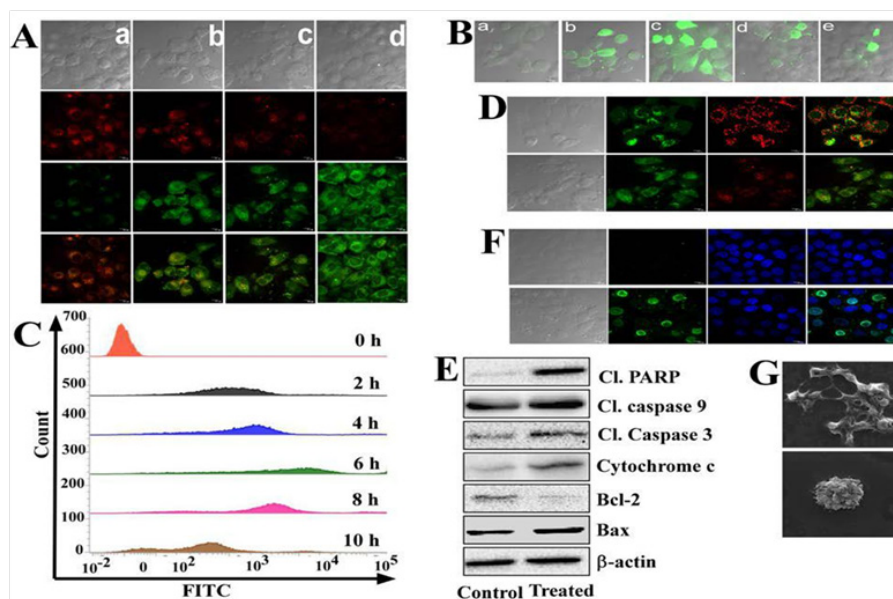
Figure S4: Flow Cytometric analysis on the effect of NFT-fMSNs induced mitochondrial membrane potential change using JC-1. (A) Uncompensated data of NIH/3T3 cells and (B) compensated data of MDA-MB-231 cells were compared with. (C) Representative confocal micrographs of MPTP after NFT-fMSNs treatment for 16 h. Control (upper panel) and treated (lower panel) MDA-MB-231 cells were loaded with calcein-AM (1 µM, green) and quencher CoCl2 (1 mM) and green fluorescence intensity of the cells were estimated. Fluorescence of treated cell mitochondria is highly reduced compared to the control. Mito tracker Red (150 nM) confirms the localization of calcein fluorescence in mitochondria. Scale bar: 10µm.

Figure S4: Flow Cytometric analysis on the effect of NFT-fMSNs induced mitochondrial membrane potential change using JC-1. (A) Uncompensated data of NIH/3T3 cells and (B) compensated data of MDA-MB-231 cells were compared with. (C) Representative confocal micrographs of MPTP after NFT-fMSNs treatment for 16 h. Control (upper panel) and treated (lower panel) MDA-MB-231 cells were loaded with calcein-AM (1 µM, green) and quencher CoCl2 (1 mM) and green fluorescence intensity of the cells were estimated. Fluorescence of treated cell mitochondria is highly reduced compared to the control. Mito tracker Red (150 nM) confirms the localization of calcein fluorescence in mitochondria. Scale bar: 10µm.

To determine whether ROS participates in NFT-fMSNs-induced apoptosis, treated MDA-MB-231 cells were probed with 2′,7′-dichlorodihydrofluoresce in diacetate (H2DCF-DA) and analyzed by CLSM Figure 5B. Maximum intracellular ROS accumulation, measured from the mean fluorescence intensity, was observed in cancerous cells at 6h post-treatment Figure 5C, whereas there was no significant intracellular ROS production in control cells. Moreover, loss of $\Delta\Psi$ m results in release of

cytochrome from mitochondria to cytosol. In the present study, mitochondrial release of cytochrome c into the cytosol of MDA-MB-231 cells was checked by staining of the treated cancer cells with MitoTracker Red.

Mitochondrial localization of cytochrome c was displayed by apunctiform staining and the apoptotic cells so formed due to release of cytochrome c into the cytosol exhibited diffuse green fluorescence Figure 5D. The release of cytochrome c into the cytosol triggers caspase-3 activation through formation of apoptosome complex. Western blot analysis shows that treatment of MDA-MB-231 cells with NFT-fMSNs resulted in increased expressions of cleaved caspase-3, cleaved caspase-9, cleaved PARP, cytochrome c and Bax, and down regulation of Bcl-2 thereby inducing apoptosis Figure 5E. Furthermore, extensive DNA degradation of the apoptotic MDA-MB-231 cells was assessed using terminal deoxynucleotidyl transferased UTP nick end labeling (TUNEL) assay.

CLSM pictures represent the number of TUNEL positive cells that increased in an intensifying manner indicating significant DNA breaks in the apoptotic cancer cells Figure 5F. Morphological changes normally associated with programmed cell death viz., membrane blebbing and apoptotic body formation in MDA-MB-231 cells following NFT-fMSNs treatment were analyzed

by SEM Figure 5G. As visualized by SEM, there are membrane protrusions apparent on the cell's outer membrane Figure 5G, left panel. It is worth pointing out that after overnight exposure to NFT-fMSNs (dose at IC50 value), cells displayed a rounded shape and prominent blebs covering the entire cell surface Figure 5G, right panel confirming cellular apoptosis.

NFT-fMSNs induces TNBC cell migration and invasion *in vitro* via IL-6/IL-6R signaling pathway

Metastasis, a dynamic hallmark of cancer, consists of three imperative events; cancer cell migration from a primary foci to secondary organ, adhesion of cancer cells at this secondary site and invasion of extracellular matrix (ECM) of secondary organ [47,48]. In the present study, treatment of MDA-MB-231 cells with NFT-fMSNs (200 and 250nM) resulted in inhibition of cell migration by 58 and 76% respectively Figure 6A and invasive ability by 63 and 38 % respectively Figure 6B suggesting the potency of NFT-fMSNs in preventing cancer cell migration and invasion. It is now an already accepted fact that inflammatory microenvironment plays crucial roles in tumor development including tumor initiation, promotion, invasion and metastasis. Gao et al. [49] in his study outlined the importance of autocrine interleukin 6 (IL-6) in lung and breast cancers and implicated IL-6 as an important activator of oncogenic STAT 3.
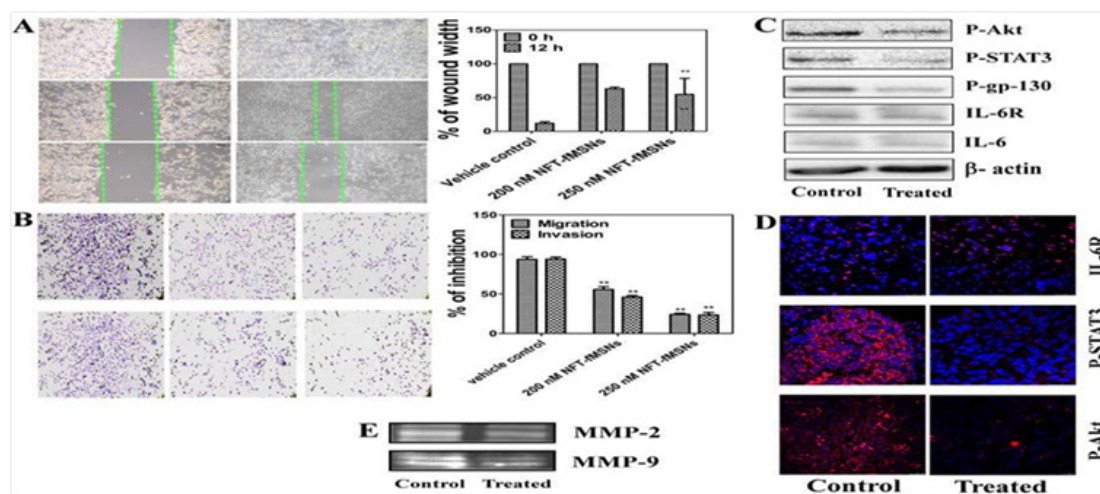

Figure 6: Representative images depict that NFT-fMSNs treatment inhibits 4T1 cell (A) migration in wound Healing assay, (B) migration (upper Panel) and invasion (lower Panel) in trans well assay in a dose dependent (200 and 250 nM)manner. Graphs represent the width of the wound and quantification of 4T1 cell migration and invasion with respect to that of vehicle control. *p< 0.05,**p< 0.01. (C) Expression of IL-6, IL-6R, P-TAT3,P-gp-130, P-Akt, was evaluated by western blot in MDA-MB-231 cells after treatment with NFT-fMSNs. (D)Immunofluorescence study of tissue sections derived from control and NFT-fMSNs- treated groups of 4T1xenograft model. Expression of P-STAT3 (upper panel) and P-Akt (middle panel) were significantly reduced in treated group whereas expression of IL-6R (lower panel) was unaltered. (E) Vehicle control and NFT-fMSNs treated conditioned media of MDA-MB-231 cells were analyzed using gelatin zymography.

In our study, western blot analysis showed NFT-fMSNs specifically suppressed IL-6 induced STAT 3 phosphorylation and Art phosphorylation due to inhibition of the binding of IL-6 to the IL-6R thereby resulting in the blockade of the IL-6/IL-6R autocrine signaling axis, responsible for tumor genesis and inflammation Figure 6C. Expression of IL-6R was almost similar in both control and NFT-fMSNs treated sets however, expression profiles of P-STAT3 and P-Akt was markedly reduced in NFT-

fMSNs-treated groups as confirmed by immune fluorescence study Figure 6D. Large number of studies have suggested that matrix metalloproteinase's, MMP-2 and MMP-9 are involved in the invasion, metastasis and poor prognosis of various cancers [50,51]. Results obtained from Gelatin zymography analyses showed that NFT-fMSNs potentially degrades MMP-2/9 production Figure 6E.

Molecular modeling

NFT is a small molecule that follows Lipinski's rule of five. Some important physico-chemical properties of this molecule and its geometry parameters are listed in the Table 3. Shape of the optimized structure and its dimensions are also shown in the Figure 7A. This molecule is around 12 Å long, 10 Å wide and 8 Å thick with asphericity index of 0.87 on a scale of 0.81 (cube) to 1.0 (sphere). To probe its binding with the extracellular domains of IL-6Rα, computation methods were employed. *In silico* molecular docking simulation showed that the interaction of NFT with IL-6Rα was thermodynamically favorable with binding energy of -23.47 k J mol-1. Apart from that, molecular docking provided insight into the most favorable binding site for NFT on the extracellular domains of IL-6Rα.

Table 3: Physico-chemical properties of nifetepimine.

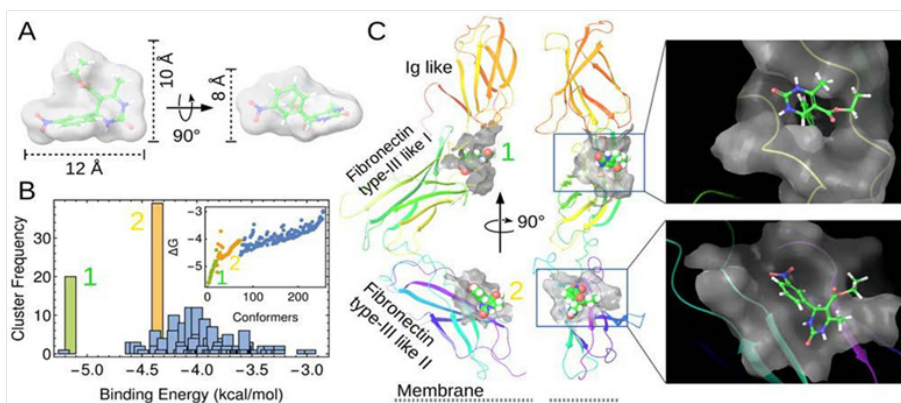| Properties	Values	Properties	Values
Log P	1.18	Solvent accessible surface area	492.47 Å2
Log S	-3.08	Vander Waals volume	258.30 Å3
Strongest acidic pKa	12.43	Sphericity (Voss and Gerstein, 2010)	0.87
Polar surface area	110.57 Å2	Effective radius	4.07 Å
Vander Waals surface area	410.93 Å2	Lipinski's rule of five	Yes

Figure7: Nifetepimine and its interaction with the extracellular domains of IL-6Rα as obtained by AutoDock4.2. (A) Dimensions of the optimized structure of nifetepimine. (B) Cluster frequency distribution of the docked S. Bhandary et al. [51] conformers of nifetepimine. Inset shows the energy distribution of all the system states (conformers) in the statistical ensemble obtained by docking simulation. Two most probable clusters are marked. (C) Arrangement of the three extracellular domains of IL-6Rα with respect to membrane and the two most probable binding sites for nifetepimine. Protein is shown in ribbon diagram and C→N terminal is colored in rainbow. Nifetepimine is shown in CPK/ball-and-stick model with standard color code for H, O and N; C is colored in green. Protein surface at the binding sites are shown in semitransparent gray.

In order to obtain a statistically significant result, genetic algorithm was run independently for 256 times and the results were clustered according to the spatial distributions and binding energy of the conformers. Two major clusters were obtained, which suggested two probable binding sites of NFT on IL-6Rα Figure 7B. The lowest energy cluster obtained by Auto Dock 4.2 showed that the binding site for NFT lay in the groove in between Ig-like N-terminal domain (domain I) and the adjacent fibronect in type-III like domain (domain II) Figure 7C.

Another binding site was obtained in the C-terminal fibronect in type-III like domain (domain III), which is close to the cell membrane. Detailed interaction diagrams of the protein–legend complex showing the interacting residues and the types of interactions obtained by molecular modeling are given in Figure 8. Best binding conformation of NFT was found to be in the groove between domain I and II of IL-6Rα Figure 7C & 8A. Leu88, Val112, Pro113, Pro114, Trp134, Pro136, Pro140, Phe174 and Val194 provide the hydrophobic environment for binding Figure 8B.

Glu115, Ser138 and Thr139 were found to form hydrogen bonding interaction with NFT. Polar amino acids Ser1417 and Thr144 also interact with the legend. Moreover, Glu115 was found to form a salt-bridge with the nitro-group of NFT. Details of the interacting residues at the two probable binding sites are highlighted in the Figure 8C. Although the binding at site 2 is a surface binding and energetically less favorable, the ligand was found to form four hydrogen bonds there with the amino acids Ile 222, Val 224 and Met 311 of the domain III ofIL-6Rα Figure

8D & 8E. Weak forces such as hydrogen bonding, hydrophobic and van der Waals interactions as well as the strong electrostatic attractions are the major players governing the binding of NFT with the extracellular domains of IL-6Rα.
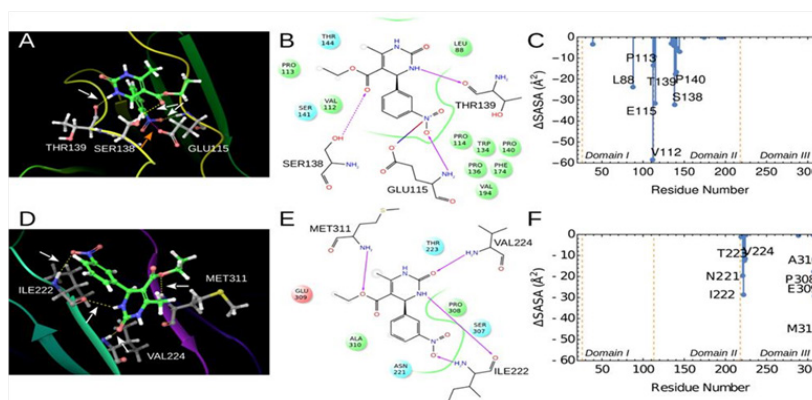

Figure 8: Interacting residues at the two most probable binding sites. (A) Orientation of the functional groups of energetically most favorable conformer of nifetepimine in the binding site groove of IL-6Rα. Protein backbone is shown in ribbon diagram. Nifetepimine and some interacting residues are shown in ball-and-stick. Standard color code used to represent the elements except C in nifetepimine, which is colored green. Hydrogen bonds are pointed with white arrowheads. Electrostatic interaction/salt Bridge is marked with red arrowhead. (B) Detailed interaction diagram of the most favorable bound state of nifetepimine with IL-6Rα. (C) Extent of solvent excision for the amino acid residues of IL-6Rα due to nifetepimine binding at site I. (D) Orientation of the functional groups of statistically most probable conformer of nifetepimine in the binding site groove of IL-6Rα. (E) Detailed interaction diagram of the most probable bound state of nifetepimine with IL-6Rα. (F) Changes in the solvent accessibility for the amino acid residues of IL-6Rα due to nifetepimine binding at site II.

Molecular docking does not directly give the solvent effects in ligand protein interactions. However, effect of solvent exclusion can be derived from the docking experiments by probing the changes in the solvent accessible surface area of protein residues and the ligand. Prior to interaction, the surface area of the ligand was 492.47 Å2 and the surface area of IL-6Rα was 16857.15 Å2. Upon complex formation the accessible surface of IL-6Rα was reduced by 228.10 and 186.54 Å2 for the two binding modes, respectively. On the other hand the ligand surface area was reduced by 70% and 54% in the two binding modes, respectively. It suggests that, at site 1 the ligand gets internalized into the groove of IL-6Rα, whereas at site 2 it remains largely solvent exposed.

The extent of changes in the solvent accessible surface area for the amino acid residues of IL-6Rα are also calculated and shown graphically in the Figure 8. Most changes in the SASA was observed for residues Leu 88, Val 112, Pro113, Glu 115, Ser 138, Thr 139, Pro 140, Asn 221, Ile 222, Thr 223, Val 224, Pro 308, Glu 309, Ala 310 and Met 311 as depicted in Figure 8. The docking study inferred that the molecule interacts strongly to the binding site of the IL-6 receptor and obstruct the binding of IL-6 with its receptor and also the formation of signaling complex with the G-protein, gp130, eventually blocking the cancer-promoting signaling pathway.

In vivo antitumor, anti-proliferation and anti-metastatic activity of NFT-fMSNs
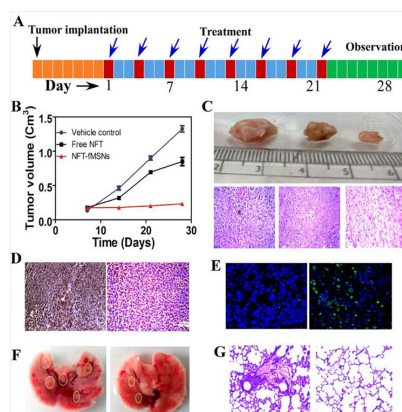

Figure 9: Panel (A) 4T1 cancer cells were subcutaneously injected to mice seven days prior to the treatment with NFT-fMSNs. These animals were received eight injections (red boxes) on every 3rd day after the first injection for 22 days. (B) Tumor growth curves after intravenous injection of NFT-fMSNs at a dose of 2.5 mg/kg body weight. Error bars indicate SEM (n=5). (C) Upper panel: Comparative photograph of the collected tumor tissues at day 28 from vehicle control (left side), free NFT treated (middle) and NFT-fMSNs treated (right side) groups and their respective H&E stained sections (lower panel) showing significant tumor inhibitory effect of NFT-fMSNs. (D) PCNA expression and (E) apoptosis in the tumor tissues in vehicle control and NFT-fMSNs treated mice groups. The tumor sections were stained with fluorescein-dUTP (green) for apoptosis and DAPI fornuclei (blue). (F) Images depict that administration of 2.5 mg/kg of NFT-fMSNs effectively suppresses spontaneous metastatic pulmonary nodule formation compared to vehicle control. (G) Respective H&E stained lung sections depict that NFT-fMSNs has effectively halt the metastatic spread in

All the *in vitro* findings encouraged us to explore *in vivo* antitumor efficacy of NFT-fMSNs, treated female BALB/c mice bearing breast tumor tissue. The optimum dose of NFT-fMSNs administration was selected to be 2.5 mg kg^{-1} body weight as obtained from serum aspartate aminotrasferase (AST) values of NFT-fMSNs treated mice (Data not shown). A month long treatment with NFT-fMSNs Figure 9A resulted in significant reduction in tumor as compared to the control group Figure 9B. Treatment with free NFT resulted in no significant reduction in tumor size. H&E images of the excised breast tumor tissues also suggest that NFT-fMSNs has a significant suppressive effect on tumor growth Figure 9C. Furthermore, PCNA staining of the excised tumor tissue sections showed that NFT-fMSNs display strong anti proliferative activity Figure 9D.

In situ TUNEL assay presented high level of apoptosis in the tumor tissues collected from NFT-fMSNs treated mice Figure 9E. Simultaneously, we made an attempt to evaluate whether NFT-fMSNs display any explicit role in inhibiting tumor invasion and metastasis. As observed in Figure 9F, a significant reduction in the number of metastatic nodules in lungs of NFT-fMSNs treated mice was noticed as compared with the vehicle treated control group. H&E images of the excised lung tissues also demonstrate that NFT-fMSNs has effectively halt the metastatic spread of breast cancer cells in lungs Figure 9G.Therefore, it can be suggested that NFT-fMSNs not only restrict primary tumor growth but also effectively halt the proliferation and metastasis.

In vivo biodistribution

The biodistribution of fluorescent mesoporous silica nanoparticles (FITC-fMSNs) was analyzed *ex vivo* on excised tissues using the Kodak Image Station 4000 MM PRO imaging system. To track FITC-fMSNs in mice bearing breast tumor, the tumor tissue and different organs viz., liver, kidney, lung, heart and spleen were excised and analyzed. The fluorescence signals from the tumor tissues were found to be much stronger than those from other organs at 4h and 24 h of FITC-fMSNs treatment respectively Figure 10A.
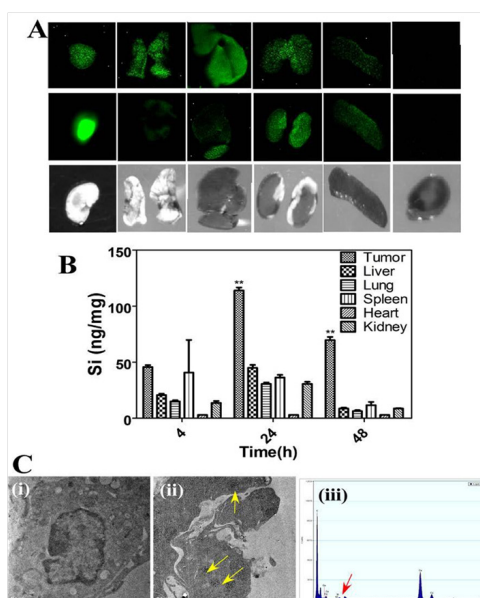

Figure 10: (A) Ex vivo fluorescence imaging of excised tumor, lung, liver, kidney, spleen and heart isolated from FITC-fMSNs treated mice. 4 h (upper panel), and 24 h (middle panel) fluorescence signal of the internalized nanoparticles from different organs and tumor is depicted here. Lower panel shows white light images. (B) ICP-OES analysis of 'Si' as organ accumulation in mg per mg of tissue post euthanasia at 4 , 24and 48 h. Data are presented as mean ± standard deviation (n =5). (C) TEM images of breast tumor tissue sections (a) control, (b) fMSNs treated showing internalization of nanoparticles (yellow arrows) after 6 h, (c) spot EDX analysis also confirms presence of silicon into the cytosol (red arrow).

Strong fluorescence intensities were found in kidneys and liver with peak fluorescence intensity being observed at 4h, followed by a gradual decrease over 48h (data not shown). Results obtained from inductively coupled plasma-optical emission spectrometry (ICP-OES) showed a significantly high Si concentration in the breast tumor tissues than that in other body organs indicating tumor targeting ability of NFT-fMSNs Figure 10B. Furthermore, TEM images along with EDX analysis of breast tumor tissues of NFT-fMSNs treated mice displayed nano clusters of NFT-fMSNs distributed in the cytoplasm Figure 10C, i-iii showing effective targeting of the nano formulation within the breast tumor tissue.

In vivo cytotoxicity of NFT-fMSNs

Images obtained from body weight analysis and H&E stained sections of lung, kidney, liver and spleen tissues of NFT-fMSNs treated mice exhibited normal morphology, thereby indicating non toxic effects of our nano formulation Figure S5. Hematology results indicate that serum parameters viz. alkaline phosphatase (ALP), alanine aminotransferase (ALT),

aspartate aminotransferase (AST), blood urea nitrogen (BUN), and creatinine were nearly to the normal level, suggesting that no inflammatory reaction was associated with NFT-fMSNs treatment (Table 4).

Table 4: Blood biochemistry results of the normal mice, tumor bearing control group of mice and tumor bearing mice treated with free NFT and NFT-MSNs. Values are as mean±SEM (n=5). ALP, alkaline phosphatase; ALT, alanine amino transferase; AST, aspartate amino transferase; BUN, blood urea nitrogen; and CRE, creatinine.

| Groups	Day	ALP(U/L)	ALT(U/L)	AST(U/L)	BUN(mg/dL)	CRE(mg/dL)
Untreated Control	7	47.51±0.07	83.53±1.23	81.05±0.9	89.9±1.9	4.55±0.5
	14	50.55±0.17	94.07±0.97	93.90±1.15	93.5±1.35	5.54±0.3
Free NFT Treated	7	3.01±0.23	89.5±2.97	77.35±0.95	63.4±1.55	3.89±0.5
	14	2.89±0.16	103.07±1.6	79.87±0.3	69.2±1.45	3.83±0.2
	21	2.67±0.55	127.78±1.5	83.79±0.79	93.5±1.5	3.69±0.5
NFT-fMSNs Treated (2.5mg/kg)	7	7.79±0.87	33.6±1.56	27.55±1.25	49.9±0.94	2.49±0.26
	14	8.72±0.47	35.1±1.89	25.70±1.85	39.3±1.25	2.3±0.5
	21	8.76±0.56	27.35±3.05	13.5±2.5	30.6±0.86	1.09±0.4
Control Without Tumor	7	5.98±0.56	23.23±0.81	11.9±0.72	29.54±0.13	0.93±0.57
	14	8.29±0.96	24.11±0.5	13.93±0.21	30.33±0.11	0.97±0.55
	21	8.38±0.28	26.7±0.22	14.57±0.9	31.02±0.1	1.03±0.47
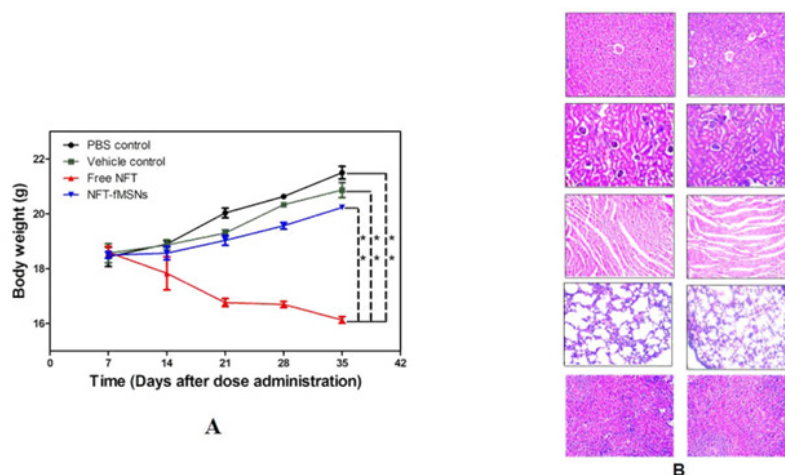
Figure S5: (A) Body weight analysis of mice of four groups. The error bars indicate mean ± SD (n = 4). (**)p < 0.01. (B) Histopathological observation of different organs (liver, kidney, heart, lung, and spleen) from tumor-bearing mice. Scale bars: 100 μm.

Discussion

The concept of targeted delivery has caught much attention in therapeutic intervention of several tumors but has been less extensively applied to metastases. It has become quintessential to direct much of the therapeutic agents to the cancer cells in order to impede invasion and metastasis. Here, we report a novel drug delivery platform with intrinsic anti-metastatic properties for the targeted delivery of the anticancer agent, NFT in treating metastatic breast cancer. NFT-fMSNs were synthesized depending on host–guest complexation between β-CD, Ada-mPEG and Ada-FA in presence of NFT.

In NFT-fMSNs, FA acts as one of the important key factors to enhance FR- mediated endocytosis by breast cancer cells. β -CD molecules have been used as gatekeepers to control the release of NFT from the pores through a pH-sensitive boronate-ester linkage, which is hydrolyzed at pH 5.0. An acid-labile benzoic-imine linkage has also been incorporated through mPEG-Ada/β-CD and FA-Ada/ β -CD complexations, offering enhancement of the DDS dispersion and cellular uptake. Physico-chemical characterizations confirm successful encapsulation of NFT and integration of functional molecules into the MSNs surfaces Figure 1. According to molecular simulation data Figure 7A, the NFT molecule scan be effectively entrapped within the cylindrical pores (a pore size of 2.98nm) of MSNs, employed as the model mesoporous nanocarrier, which is more than two times larger than the size of NFT molecule.

Entrapment efficiency of NFT-Ns was found to be almost 80%. *In vitro* results Figure 2 indicate that the drug loading and release capacity of fMSNs is heavily dependent on the introduction of pH-operated β-CD nano valves and PEGylation of NFT-fMSNs resists protein adsorption, improves biocompatibility, and increases *in vivo* circulation time with better resilience via a pH-sensitive benzoic-imine linkage.

The TGA curves indicate that around 14wt% of NFT was loaded into fMSNs system, which corresponds to the result (16 wt %) obtained by equation 1. Figure 2A shows that at neutral pH, stable boronic acid-catechol ester bonds prevented rapid release of the entrapped cargo and the cleaved linkers under pH 6.8 indicates sustained drug release (23%). Moreover, most of the linkers were found to be broken down when exposed to endosomal pH leading to β-CD dissociation from fMSNs and pH-dependent controlled release of NFT (74%) over a period of 24 h. Figure 3B shows that cellular uptake of fMSNs was higher at pH 6.8 than that at pH 7.4 because dissociation of the benzoic-imine linkers between MSNs and mPEG molecules occurs under acidic condition.

Following cleavage of mPEG shell, surface bioactive molecules, Ada and FA, became exposed and facilitated cellular internalization of fMSNs. Therefore, our strategy was to use this novel approach in designing a pH-sensitive nano formulation that can successfully trigger targeted release of NFT with maximum therapeutic effect and minimum side-effects. Therapeutic potential of NFT-fMSNs against breast cancer can be well established from the apoptotic activities of the nano formulation in TNBC cells via caspase dependent pathway Figure 4 & 5.

Loss of $\Delta\Psi$ m and subsequent release of cytochrome c, followed by caspase-3 activation and cleavage of PARP resulted in apoptosis of cancer cells. On the basis of these encouraging results, we sought to explore the anti-tumorigenic activities of NFT-fMSNs in female BALB/c mice bearing breast tumor. Significant reduction in breast tumor volume was observed upon treatment with NFT-fMSNs Figure 9B. The antitumor efficacy of NFT-fMSNs might be accredited to the tumor-preferential accumulation of NFT-fMSNs in breast tumor bearing mice, presumably due to EPR effect and FR-targeting.

Improvement in body weight was also observed in NFT-fMSNs treated tumor bearing mice when compared to the control group of mice Figure S5A. Increased invasiveness within the tumor microenvironment is associated with inflammation leading to poor prognosis in breast cancer [52]. Evidences suggest that inflammatory cytokine, IL-6, assumes a direct role in the up regulation of malignant features in breast cancer cells [53-55]. Results from our study indicated that targeted inhibition of IL-6/IL-6R-mediated Stat3 and Akt signaling by NFT-fMSNs might provide an insight into the therapeutic intervention of TNBC. Results from docking analysis Figure 7 & 8 further confirmed that the targeted inhibition of IL6/IL-6R occurred due to the strong interaction of NFT with the binding site of IL-6R, finally blocking the progression of cancer.

The expression and predictive significance ofMMP-2 and MMP-9 has not yet been fully elucidated, but recent studies have shown that increased gelatin as expression in the primary tumor can be linked with aggressiveness of the cancer cells [56,57]. In our study, NFT-fMSNs potentially degrades MMP-2/9 production both *in vitro* and *in vivo* thereby drawing a strong correlation among cancer cell invasion, tumor growth and metastasis Figure 6E. Taken together, these findings help in understanding the mechanisms involved behind the successful targeting of an anticancer agent via fMSNs and subsequent inhibition of breast cancer cell invasion and metastasis. However, other prognostic factors need to be attended and clinical trials should be undertaken in order to understand the role of NFT-fMSNs in specific targeting of the immune system and inflammation in triple negative breast carcinoma.

Conclusion

In summary, a new generation nanocarrier based on MSNs has been developed based on the doctrines of supra molecular chemistry, nanoscale fabrication and pH- responsive operation that can be used as a promising candidate for improved breast cancer therapy. Furthermore, we have shown how functionalized MSNs with supra molecular ensembles on their external surface and targeting ligands are capable of on-demand release of their entrapped guest (NFT) upon pH modulations.

Comprehensive studies regarding to the controlled release and local delivery of therapeutics and the appraisal of cytotoxicity have validated the feasibility of NFT-fMSNs as an efficient delivery system of poorly water soluble drugs to breast cancer cells. An increase is observed in nanocarrier uptake and cellular apoptosis in TNBC cells at very low doses of FA modified NFT-fMSNs when compared to NFT-fMSNs without FA-modification. The results here provide a potential strategy to treat an aggressive form of TNBC and also indicated that targeting IL-6R may be a useful strategy to restraint tumor invasion and metastasis.

We believe this study will aid in designing intravenous drug delivery systems for target specific release of poorly water soluble drugs and especially highlight the global need for efficient and secure chemotherapeutic agents that have the capability to target tumors like breast cancer with minimum adverse effects. For future applications these functionalized nanocarriers may provide new hope in treating metastatic breast cancer with better therapeutic efficacy. Although our preliminary results strengthen the notion that targeting of the IL-6 system inhibits metastatic progression of breast carcinoma but, future clinical studies is required to validate these conclusions.

References

1. Kassam F, Enright K, Dent R, Dranitsaris G, Myers J, et al. (2009) Survival Outcomes For Patients With Metastatic Triple-Negative Breast Cancer: Implications For Clinical Practice And Trial Design. Clin Breast Cancer 9(1): 29-33.

2. Han L, Huang R, Li J, Liu S, Huang S, et al. (2011) Plasmid pORF-hTRAIL and doxorubicin co-delivery targeting to tumor using peptide-conjugated polyamidoamine dendrimer. Biomaterials 32(4): 12421252.

3. Ghosh S, Adhikary A, Chakraborty S, Bhattacharjee P, Mazumdar M, et al. (2015) Cross-talk between ER stress and the MEK/ERK pathway potentiates apoptosis in human triple-negative breast carcinoma cells: Role of a dihydropyrimidone, Nifetepimine, J Biol Chem 290: 3936-3949.

4. Ghosh A, Bhowmik A, Bhandary S, Putatunda S, Laskar A, et al. (2016) Formulation and antitumorigenic activities of nanoencapsulated nifetepimine: A promising approach in treating triple negative breast carcinoma, Nanomedicine 12(7): 1973-1985.

5. Zhao Y, Trewyn BG, Slowing II, Lin VS (2009) Mesoporous silica nanoparticle-based double drug delivery system for glucose-responsive controlled release of insulin and cyclic AMP, J Am Chem Soc 131(24): 8398-8400.

6. Klichko Y, Liong M, Choi E, Angelos S, Nel AE, et al. (2009) Mesostructured Silica for Optical Functionality, Nanomachines, and Drug Delivery. J Am Ceram Soc 92(s1): s2-s10.

7. Lu J, Choi E, Tamanoi F, Zink JI (2008) Light-Activated Nanoimpeller-Controlled Drug Release in Cancer Cells. Small 4(4): 421-426.

8. Mura S, Nicolas J, Couvreur P (2013) Stimuli-responsive nanocarriers for drug delivery. Nat Mater 12(11): 991-1003.

9. Liu R, Zhang Y, Zhao X, Agarwal A, Mueller LJ, et al. (2010) pH-responsive nanogated ensemble based on gold-capped mesoporous silica through an acid-labile acetal linker. J Am Chem Soc 132(5): 1500-1501.

10. Lankveld DP, Rayavarapu RG, Krystek P, Oomen AG, Verharen HW et al. (2011) Blood Clearance and Tissue Distribution of PEGylated and NonPEGylated Gold Nanorods after Intravenous Administration in Rats. Nanomedicine (Lond) 6(2): 339-349.

11. Hatakeyama H, Akita H, Harashima H (2011) A multifunctional envelope type nano device (MEND) for gene delivery to tumours based on the EPR effect: A strategy for overcoming the PEG dilemma. Adv Drug Deliver Rev 63(3): 152-160.

12. Zhang Z, Wang J, Tacha DE, Li P, Bremer RE, et al. (2014) Folate Receptor a Associated With Triple-Negative Breast Cancer and Poor Prognosis. Arch Pathol Lab Med 138(7): 890-895.

13. O'Shannessy DJ, Somers EB, Maltzman J, Smale R, Fu YS (2012) Folate receptor alpha (FRA) expression in breast cancer: identification of a new molecular subtype and association with triple negative disease. Springer plus 1: 22.

14. Wang Z, Xu B, Zhang L, Zhang J, Ma T, et al. (2013) Folic acid-functionalized mesoporous silica nanospheres hybridized with AIE luminogens for targeted cancer cell imaging. Nanoscale 5(5): 2065-2072.

15. Gao W, Xiang B, Meng TT, Liu F, Qi XR (2013) Chemotherapeutic drug delivery to cancer cells using a combination of folate targeting and tumor microenvironment-sensitive polypeptides. Biomaterials 34(16): 4137-4149.

16. Leamon CP, Reddy JA (2004) Folate-targeted chemotherapy. Adv Drug Deliv Rev 56(8): 1127-1141.

17. Qing Yang, Shichao Wang, Peiwei Fan, Lifeng Wang, Yan Di, et al. (2005) pH-Responsive carrier system based on carboxylic acid modified mesoporous silica and polyelectrolyte for drug delivery. Chem Mat 17(24): 5999-6003.

18. Park C, Oh K, Lee SC, Kim C (2007) Controlled release of guest molecules from mesoporous silica particles based on a pH-responsive polypseudorotaxane motif. Angew Chem Int Ed 46(9): 1455-1457.

19. Liu J, Luo Z, Zhang J, Luo T, Zhou J (2016) Hollow mesoporous silica nanoparticles facilitated drug delivery via cascade pH stimuli in tumor microenvironment for tumor therapy. Biomaterials 83: 51-65.

20. ong DS, Angelo LS, Kurzrock R (2007) Interleukin-6 and its receptor in cancer: implications for translational therapeutics.

21. Cancer 110(9): 1911-1928.

22. Conze D, Weiss L, Regen PS, Bhushan A, Weaver D, et al. (2001) Autocrine production of interleukin 6 causes multidrug resistance in breast cancer cells. Cancer Res 61(24): 8851-8858.

23. Walter M, Liang S, Ghosh S, Hornsby PJ, Li R (2009) Interleukin 6 Secreted from Adipose Stromal Cells Promotes Migration and Invasion of Breast Cancer Cells. Oncogene 28(30): 2745-2755.

24. Dirat B, Bochet L, Dabek M, Daviaud D, Dauvillier S, et al. (2011) Cancer-associated adipocytes exhibit an activated phenotype and contribute to breast cancer invasion. Cancer Res 71(7): 2455-2465.

25. Salgado R, Junius S, Benoy I, Van Dam P, Vermeulen P, et al. (2003) Circulating interleukin-6 predicts survival in patients with metastatic breast cancer. Int J Cancer 103(5): 642-646.

26. Gupta GP, Nguyen DX, Chiang AC, Bos PD, Kim JY, et al. (2007) Mediators of vascular remodeling co-opted for sequential steps in lung metastasis. Nature 446(7137): 765-770.

27. Deryugina EI, Quigley JP (2006) Matrix metalloproteinases and tumor metastasis. Cancer Metastasis Rev 25(1): 9-34.

28. Ji T, Zhao Y, Ding Y, Nie G (2013) Using functional nanomaterials to target and regulate the tumor microenvironment: diagnostic and therapeutic applications. Adv Mater 25(26): 3508-3525.

29. Rundhaug JE (2003) Matrix Metalloproteinases, Angiogenesis and Cancer commentary re: A. C. Lockhart et al., Reduction of wound angiogenesis in patients treated with BMS-275291, a broad spectrum matrix metalloproteinase inhibitor. Clin. Cancer Res., 9: 00-00, 2003. Clin Cancer Res 9(2): 551-554.

30. Biginelli P (1893) Aldehyde-urea derivatives of aceto- and oxaloacetic acids. Gazz Chem Ital 23: 360-413.

31. Ghosh S, Adhikary A, Chakraborty S, Nandi P, Mohanty S, et al. (2012) Nifetepimine, a Dihydropyrimidone, Ensures CD4+ T Cell Survival in a Tumor Microenvironment by Maneuvering Sarco(endo)plasmic Reticulum Ca2+ ATPase (SERCA). J Biol Chem 287(39): 32811-32896.

32. Nooney RI, Thirunavukkarasu D, Chen YM, Josephs R, Ostafin AE (2002) Synthesis of nanoscale mesoporous silica spheres with controlled particle size. Chem Mater 14(11): 4721-4728.

33. Karaman DS, Desai D, Senthilkumar R, Johansson EM, Råtts N et al. (2012) Shape engineering vsorganic modification of inorganic nanoparticles as a tool for enhancing cellular internalization. Nanoscale Res Lett 7(1): 358.

34. Trewyn BG, Nieweg JA, Zhao Y, Lin VSY (2008) Biocompatible mesoporous silica nanoparticles with different morphologies for animal cell membrane, penetration. Chem Eng J 137: 23-29.

35. Luo Z, Cai K, Hu Y, Zhang B, Xu D (2012) Cell specific intracellular anticancer drug delivery from mesoporous silica nanoparticles with pH sensitivity. Adv Healthc Mater 1(3): 321-325.

36. Pan X, Chen Y, Zhao P, Liu Z (2015) Highly efficient solid phase labelling of saccharides within boronic acid functionalized Mesoporous silica nanoparticles. Angew Chem Int 54(21): 6173-6176.

37. Takahashi K, Hattori K, Toda F (1984) Monotosylated α-and β-cyclodextrins prepared in an alkaline aqueous solution. Tetra hedron Lett 25: 3331-3334.

38. Petter RC, Salek, JS, Sikorsky CT, Kumaravel G, Lin FT (1990) Cooperative binding by aggregated mono-6-(alkylamino)-β-cyclodextrins. J Am Chem Soc 112(10): 3860-3868.

39. Luo Z, Hu Y, Cai K, Ding X, Zhang Q (2014) Intracellular redox-activated anticancer drug delivery by functionalized hollow mesoporous silica nanoreservoirs with tumor specificity. Biomaterials 35(27): 7951-7962.

40. Wang XG, Dong ZY, Cheng H, Wan SS, Chen WH, et al. (2015) A multifunctional metal-organic framework based tumor targeting drug delivery system for cancer therapy. Nanoscale 7(38): 16061-16070.

41. Wang H, Wang S, Su H, Chen KJ, Armijo AL et al. (2009) A supramolecular approach for preparation of size-controlled nanoparticles. Angew Chem Int Ed Engl 48(24): 4344-4348.

42. Ang CY, Tan SY, Wang X, Zhang Q, Khan M, et al. (2014) supramolecular nanoparticle carriers self assembled from cyclodextrin- and adamantine functionalized polyacrylates for tumor-targeted drug delivery. J Mater Chem B 2: 1879-1890.

43. Chandran P, Sasidharan A, Ashokan A, Menon D, Nair S (2011) Highly biocompatible TiO_2:Gd^{3+} nano-contrast agent with enhanced longitudinal relaxivity for trgeted cancer imaging. Nanoscale 3: 4150-4161.

44. Lin YS, Haynes CL (2010) Impacts of mesoporous silica nanoparticle size, pore ordering, and pore integrity on hemolytic activity. J Am Chem Soc 132(13): 4834-4842.

45. Migliore L, Nieri M, Amodio S, Loprieno N (1989) The human lymphocyte micronucleus assay: a comparison between whole-blood and separated-lymphocyte cultures. Mutat Res 227(3): 167-172.

46. Ojha PK, Roy K (2010) Chemometric modeling, docking and in silico design of triazolopyrimidine-based dihydroorotate dehydrogenase inhibitors as antimalarials. Eur J Med Chem 45(10): 4645-4656.

47. Varghese JN, Moritz RL, Lou MZ, Van Donkelaar A, Ji H, et al. (2002) Structure of the extracellular domains of the human interleukin-6 receptor alpha -chain. Proc Natl Acad Sci 99: 15959-15964.

48. Walter M, Liang S, Ghosh S, Hornsby PJ, Li R (2009) Interleukin 6 Secreted from Adipose Stromal Cells Promotes Migration and Invasion of Breast Cancer Cells. Oncogene 28(30): 2745-2755.

49. Gupta GP, Massague J (2006) Cancer metastasis: building a framework. Cell 127: 679-695.

50. Gao SP, Mark KG, Leslie K, Pao W, Motoi N et al. (2007) Mutations in the EGFR kinase domain mediate STAT3 activation via IL-6 production in human lung adenocarcinomas, J Clin Invest 117(12): 3846-3856.

51. Kallakury BV, Karikehalli S, Haholu A, Sheehan CE, Azumi N, et al (2001) Increased expression of matrix metalloproteinases 2 and 9 and tissue inhibitors of metalloproteinases 1 and 2 correlate with poor prognostic variables in renal cell carcinoma, Clin Cancer Res 7(10): 3113-3119.

52. M. Libra, A. Scalisi, N. Vella, R. Clementi, R. Sorio, et al (2009) Uterine cervical carcinoma: role of matrix metalloproteinases (review). Int J Oncol 34(4): 897-903.

53. Goldberg JE, Schwertfeger KL (2010) Proinflammatory cytokines in breast cancer: mechanisms of action and potential targets for therapeutics. Curr Drug Targets 11(9): 1133-1146.

54. Esquivel-Velázquez M, Ostoa-Saloma P, Palacios-Arreola MI, Nava-Castro KE, Castro JI, et al. (2015) The role of cytokines in breast cancer development and progression, J Interferon Cytokine Res 35(1): 1-16.

55. Lin S, Gan Z, Han K, Yao Y, Min D (2015) Interleukin-6 as a prognostic marker for breast cancer: a meta-analysis. Tumori 101(5): 535-541.

56. Ara T, Declerck YA (2010) Interleukin-6 in Bone Metastasis and Cancer Progression. Eur J Cancer 46(7): 1223-1231.

57. Scorilas A, Karameris A, Arnogiannaki N, Ardavanis A, Bassilopoulos P, et al. (2001) Over expression of matrix-metalloproteinase-9 in human breast cancer: a potential favorable indicator in node negative patients. Br J Cancer 84(11):1488-1496.

Your next submission with JuniperPublishers will reach you the below assets

- Quality Editorial service
- Swift Peer Review
- Reprints availability
- E-prints Service
- Manuscript Podcast for convenient understanding
- Global attainment for your research
- Manuscript accessibility in different formats
  (Pdf, E-pub, Full Text, Audio)
- Unceasing customer service

Track the below URL for one-step submission
https://juniperpublishers.com/submit-manuscript.php